aerospace

MDPI

Article

Incremental MPC-Based Maneuver Method for Gliding Vehicle Under Uncertain Dynamic Constraints

Zhengquan Liu, Haitao Song *, Xiafu Wang, Shaobo Wang, Yang Guo and Yongchao Wang

Graduate School, Rocket Force University of Engineering, Xi'an 710025, China; liuzhengquan0910@163.com (Z.L.); wangxiafu@163.com (X.W.); wangshaobo0325@163.com (S.W.); guoyang820@foxmail.com (Y.G.); ycwang9103@126.com (Y.W.)

* Correspondence: songht1018@163.com

Abstract

This paper investigates an active interference strategy for gliding vehicles subject to uncertain dynamic constraints, with modeling based on optimal control. A gliding vehicle executes evasive maneuvers to actively interfere with the radar systems' trajectory estimation and prediction, which employs the Singer model combined with an extended Kalman filter (EKF). Distinct from existing studies that primarily adopt threat-zone circumvention strategies, this paper proposes an incremental model predictive control (IMPC)-based maneuver method for gliding vehicle, enabling quantitative analysis of the radar systems' trajectory estimation and prediction process with the objective of generating sufficiently large prediction errors. First, based on the time-scale separation (TSS) principle, the nonlinear flight dynamics are transformed into a weakly model-dependent incremental linear dynamic system. Second, the error bounds of the incremental linearization are established, and the system is discretized. On this basis, under multiple uncertain dynamic constraints, the IMPC-based maneuver method is developed to maximize the radar system's prediction errors during the detection and tracking phase. Finally, numerical simulations are conducted to examine the effectiveness and computational cost of the proposed strategy.

Keywords: active interference strategy; incremental model predictive control; multiple constraints

1. Introduction

As the initial phase of interception in radar systems, the detection and tracking segment is primarily responsible for monitoring, tracking, and predicting the trajectory of the target vehicle and for transmitting real-time motion information to the interceptor so as to guide it toward the predicted intercept point [1,2]. A typical gliding vehicle operates at altitudes ranging from 20 km to 60 km during the gliding phase, and this flight phase usually lasts for a relatively long duration [3,4]. Owing to its extremely high flight velocity, the vehicle generates intense shock waves and a plasma sheath, which can significantly enhance its radar cross-section (RCS) and make it particularly susceptible to detection and tracking by hostile radar early-warning systems. Due to the long-duration gliding characteristics and high vulnerability to early-warning detection, this gliding phase constitutes the key stage for interception by radar systems. Accordingly, the active survivability strategy and method for gliding vehicles are investigated in this paper, whereby maneuver control is employed to interfere with radar systems interception and thereby enhance the survivability effectiveness of the gliding vehicle.

Check for updates

Academic Editor: Mostafa Hassanalian

Received: 15 October 2026
Revised: 10 November 2026
Accepted: 14 November 2026
Published: 23 November 2026

Copyright: © 2026 by the authors. Licensee MDPI, Basel, Switzerland. This article is an open access article distributed under the terms and conditions of the Creative Commons Attribution (CC BY) license.

Currently, gliding vehicles adopt two main maneuver strategies to counter detection threats posed by radar systems: one is the no-fly zone avoidance strategy, and the other is the active interference strategy during the detection phase [5,6]. The first strategy leverages the large-scale maneuvering capability of the vehicle to evade radar detection, which is achieved through trajectory planning and reentry guidance [7,8]. Such methods involve continuously updating the heading angle error corridor for no-fly zone avoidance according to the detection coverage of multiple threat regions. The associated algorithms are well-established, computationally efficient, and exhibit superior real-time performance, thus rendering this approach the most extensively studied and widely applied. Liang [9] and Zhang [10] proposed a predictor–corrector guidance scheme integrated with no-fly zone avoidance, where algorithms were designed for the longitudinal and lateral channels respectively to control the bank angle. In ref. [11], a waypoint-planning maneuver guidance strategy based on virtual multi-tentacle detection was presented, which effectively handled multiple constraints in the maneuver guidance process. Wang et al. [12] proposed a composite differential game guidance scheme for three-player attack–defense engagement with static obstacles, accounting for energy, overload and obstacle constraints. In ref. [13], an optimization algorithm for maneuver trajectories of air-breathing gliding vehicles was developed. It is noteworthy that the above studies [7,9–11,13] adopt drastic lateral maneuvers; however, these maneuvers lead to reduced downrange capability and terminal velocity loss.

In view of the disadvantages brought about by drastic lateral maneuvers, active interference strategies have garnered growing research attention. This strategy mainly employs specific evasive maneuvers to interfere with the detection and tracking process of radar systems, degrading radar systems' tracking accuracy and ultimately leading to interceptor launch failure or post-launch misguidance. A robust integrated guidance and control law was designed in ref. [14], where a serpentine maneuvering acceleration command was introduced as a bias term. Ref. [15] proposed two lateral oscillatory maneuvering strategies to counter radar systems and interceptor missiles, respectively. Nevertheless, such maneuvering methods fail to quantitatively analyze the detection and tracking process of radar systems, making it impossible to accurately characterize maneuver effectiveness. For the quantitative analysis of detection performance, Guo et al. [16,17] proposed a quantitative maneuver design framework that considered the detection performance of interceptor systems. A model predictive control (MPC)-based maneuver method [18–21] was further developed. It adopts position-prediction error as the performance metric, aiming to maximize the prediction error of the interceptor. When designing active interference maneuvers, the flight dynamics of gliding vehicles are subject to considerable nonlinearity, strong coupling, and atmospheric disturbances. These factors introduce dynamic uncertainty in the form of unmodeled dynamics and parameter perturbations, which degrade the performance of conventional model-dependent MPC methods [22,23]. The presence of such uncertain constraints necessitates a control approach that achieves robust performance without relying on precise knowledge of the full nonlinear dynamics. To address this issue, an incremental model predictive control (IMPC) strategy combined with time-delay estimation was proposed by Wang et al. [24,25], offering a new approach to constrained control with unknown dynamics. The incremental formulation inherently reduces sensitivity to model uncertainties by exploiting high-frequency state measurements, thereby enabling robust maneuver control without requiring precise knowledge of the complete nonlinear dynamics. Ref. [26] proposed a real-time fault-tolerant guidance method that jointly reconstructs the degraded orbit and flight trajectory via sequential convex programming (SCP) and accommodates parameter deviations and external disturbances with a receding horizon strategy. Accordingly, a maneuver control method for the gliding vehicle

is designed within the IMPC framework, which reduces the dependence on an accurate model and enables quantitative analysis of the maneuver effectiveness, thereby constituting a feasible active interference strategy for gliding vehicles. It should be noted that the design of any active interference strategy first relies on an accurate model of the radar's detection and tracking segment, whose core, in essence, is maneuvering target tracking.

Maneuvering target tracking research primarily focuses on three core aspects: target maneuver models, state filtering, and state prediction, with the maneuver model serving as the foundation of the latter two. Conventional CV and CA models assume constant velocity and constant acceleration, and thus are incapable of accurately tracking gliding vehicles. To address this, the Singer model defined target acceleration as a time-varying zero-mean first-order Markov process [27], but its tracking accuracy deteriorates under drastic maneuvers. Moose et al. [28] later proposed a semi-Markov model for target acceleration. For the complex motion of near-space gliding vehicles, a damped oscillation model was constructed by compensating the zero-mean random acceleration with an oscillating function, and in combination with the Kalman filter, it achieved high-precision position prediction [29]. Fast multiple model adaptive estimation was adopted in refs. [30,31] to solve the state estimation problem of targets with randomly switching maneuvers. All these approaches model target acceleration through maneuver-driven models and then estimate or predict the target state via filtering. Consequently, a maneuvering-target tracking model can be constructed by combining classical maneuver models with filtering methods, which enables the estimation and prediction of the target position and provides a baseline for comparison in the quantitative analysis of maneuver effectiveness. In addition, when tracking a maneuvering target, factors such as parameter uncertainties and external disturbances impose more stringent requirements on controller robustness. Ref. [32] proposed a backstepping-based robust adaptive control strategy, in which an adaptive law is constructed to estimate online the norm bound of the unknown, state-dependent uncertainty, and the boundary layer technique is adopted to eliminate control chattering. Bianchi et al. [33] designed a nonlinear robust controller based on a high-order sliding mode estimator, which ensures asymptotic tracking of position and yaw by estimating and compensating for model parameter variations and time-varying wind disturbances. Compared with non-robust control, the robust controller yields smaller tracking errors and lower actuation energy consumption in target tracking.

Motivated by the above analysis, this paper proposes a maneuver control method for gliding vehicles under uncertain dynamic constraints. By quantitatively analyzing the maneuver effectiveness in the detection and tracking process, the proposed IMPC-based approach achieves robust performance against model uncertainties while satisfying multiple dynamic constraints. The main contributions of this paper compared with existing researches are summarized as follows:

1. By introducing the time-scale separation (TSS) principle, the nonlinear guidance and control system is converted into an incremental linear dynamic system with a cascaded control structure in this paper. Driven by high-frequency sensor state measurements, this incremental formulation inherently reduces sensitivity to model uncertainties and characterizes system dynamic variations in incremental form, thereby reducing reliance on the nonlinear guidance system models compared with refs. [8,12,13].
2. This paper relates the maneuver effectiveness of gliding vehicles to the interference imposed on the tracking and prediction procedures of radar systems, and formulates a prediction error cost function to characterize radar detection performance. Nonlinear process constraints under dynamic uncertainty are processed in an incremental manner and further transformed into state constraints that do not rely on the exact nominal model. Compared with the conventional nonlinear-optimization-based MPC

formulation [20,21], the IMPC framework reduces the computation time per control update and the reliance on the nominal model, at the cost of a slightly lower peak prediction error.

3. The maneuver control problem under uncertain dynamic constraints is formulated as a multi-constrained optimal control problem. Based on the aforementioned incremental linear system with a cascaded control structure, an IMPC-based maneuver control method is developed by integrating both control and state constraints. The control input derived from this method can maximize the prediction errors of radar systems under uncertain dynamics, and avoid the loss of flight range and terminal speed compared with violent lateral maneuvers [7,15,34].

The organization of this paper is as follows: Section 2 presents the problem formulation and establishes the models for radar systems and gliding vehicle. In Section 3, the main results are elaborated on. Section 4 examines the effectiveness and computational cost of the proposed method from multiple perspectives through numerical simulations. Finally, Section 5 concludes this paper.

2. Problem Formulation

This section constructs the mathematical models underlying the proposed evasive maneuver strategy. The problem formulation is split into two components. First, a mathematical model is established for radar detection and tracking, in which the Singer model combined with an extended Kalman filter is utilized to characterize the mechanism of target state estimation and prediction. Second, the dynamic model of the gliding vehicle is presented, consisting of point-mass flight kinematics, aerodynamic formulations and various trajectory constraints. These integrated models reproduce the core characteristics of the intercept-evasion engagement and lay a theoretical foundation for subsequent incremental linearization and maneuver controller synthesis.

2.1. Model of Radar Systems

This paper focuses on the radar systems' detection and tracking phase of gliding vehicles, as illustrated in Figure 1. The positions of a gliding vehicle are mainly tracked by radar systems, whose predicted positional data are transmitted to interceptors to steer them toward the computed intercept point. As the tracking and prediction accuracy of the position information supplied by radar systems improves, the interception probability of a gliding vehicle is increased accordingly; conversely, such probability is reduced. Accordingly, this paper proposes a gliding vehicle maneuver strategy for the radar systems' detection and tracking phase.

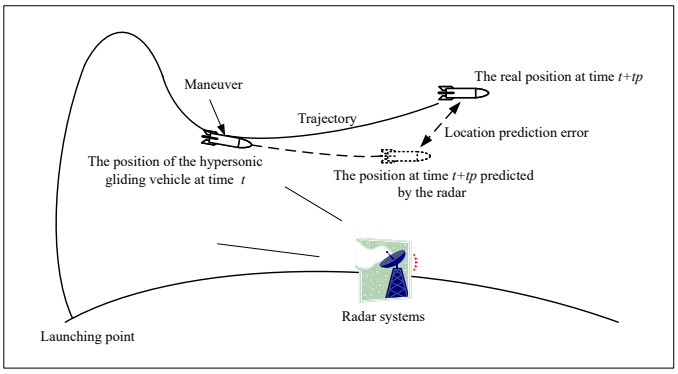

Figure 1. Schematic of radar systems' detection and tracking phase.

The gliding vehicle executes a maneuver at time t, which induces a sufficiently large prediction error in the position estimate of the vehicle at time $t + tp$ generated by the radar

systems. These prominent errors are caused to breach the launch error threshold for valid interception or give rise to post-launch guidance deviations. Consequently, the gliding vehicle successfully completes evasive maneuvering and avoids interception.

Radar systems are employed to estimate and predict the state information of gliding vehicles based on real-time measurement data, and such predicted state information is then used to guide interceptors toward targets for interception. In actual maneuvering scenarios, the measurement data accessible to radar systems mainly include the relative distance to gliding vehicles, longitudinal line-of-sight (LOS) angle and lateral LOS angle. The core objective of this paper is to explore effective maneuver strategies capable of interfering with the detection and tracking processes of radar systems. For this purpose, the Singer model, a classic and widely adopted model for maneuvering targets, together with the EKF, is adopted to simulate the target state tracking and prediction mechanism of radar systems.

Before establishing the relative kinematic equations, the following assumptions are made in this paper.

Assumption 1. *The Earth is assumed to be a stationary inertial frame and Earth rotation effects on the vehicle trajectory are ignored.*

Remark 1. *Assumption 1 is widely adopted in maneuver strategy design, and the results in refs. [5,13,15,22] are all based on this assumption. Since this paper focuses on maneuvering and guidance strategies, under the given flight conditions, the equivalent load factor of the Coriolis force arising from Earth's rotation is of a magnitude sufficiently small relative to the available load factor of the glide vehicle. Therefore, the trajectory deviation caused by Earth's rotation is negligible. This assumption simplifies the kinematic model and reduces the difficulty of algorithm design and numerical computation.*

Assumption 2. *The gliding vehicle is modeled as a point mass with lag-free dynamics [35].*

Remark 2. *Assumption 2 applies generally to trajectory planning and guidance law simulation [9–11]. A point-mass representation simplifies the dynamic analysis and reduces computational complexity, with negligible impact on the design and validation of the guidance law. In addition, the response time constant of modern guidance systems is typically on the order of tens of milliseconds, whereas the critical time scale of the guidance process is on the order of seconds, so the two differ by one to two orders of magnitude, implying that the control loop responds much faster than the guidance commands vary. Consequently, the time-delay effects are insignificant relative to the critical time scale of the guidance process, and the control loop can be treated as an ideal, delay-free element in the guidance law design.*

Based on the above assumptions, the acceleration $a_i(t),\ i \in \{x, y, z\}$ of the gliding vehicle is characterized as a zero-mean first-order Markov process by the Singer model, whose explicit formulation is given as follows:

$$\dot{a}_i(t) = -\alpha_i a_i(t) + \omega_i(t), \tag{1}$$

where α_i denotes the different maneuver methods of the gliding vehicle. The term $\omega_i(t),\ i \in \{x, y, z\}$ represents additive white Gaussian noise (AWGN) with zero mean and power spectral density of $2\alpha_i\sigma_\alpha^2$, where σ_α denotes the standard deviation of the noise.

Assumption 3. *The gliding vehicle moves with continuously varying velocity and acceleration, no impulsive change occurring in either of them; its acceleration is described by the continuous-time first-order Markov process in Equation (1), whose maneuver frequency α_i and acceleration standard*

deviation σ_α $(i = x, y, z)$ are known positive constants, constant over the whole tracking and prediction window, and whose driving noise $\omega_i(t)$ is zero-mean white Gaussian with power spectral density $2\alpha_i\sigma_\alpha^2$, mutually independent over the three axes and independent of both the initial state and the measurement noise $\zeta(t)$.

Remark 3. *Equation (1) is understood in the Itô sense, i.e., $\omega_i(t)$ is the formal derivative of a Wiener process, so that $a_{H,i}(t)$ is continuous but not classically differentiable and Equations (1)–(3) are used only in their discretized form, Equation (4). The continuity of the acceleration is not postulated but follows from unpowered flight and the bank-rate limit $|\dot{\sigma}_\mathrm{H}| \leq \dot{\sigma}_{\mathrm{H,max}}$ in Equation (9), which preclude a jump in the control-induced acceleration; since the step T is two orders of magnitude smaller than both $1/\alpha$ and t_p, the intra-step variation of the state is negligible. The parameter $\alpha_i = 1/\tau_i$ is the reciprocal of the maneuver time constant, with $\alpha_i \to 0$ recovering the constant-acceleration model and $\alpha_i \to \infty$ the constant-velocity model, and $\alpha_x = \alpha_y = \alpha_z = 0.01\ \mathrm{s}^{-1}$ is used here. It is not estimated online, the radar being assumed to possess prior knowledge of the target maneuver method, as is standard for Singer-model-based tracking [27]. Since α_i enters only the radar model, Equations (1)–(7), and neither the vehicle dynamics in Equation (8) nor the IMPC problem in Equations (58)–(63), this assumption leaves the feasibility of the maneuver unaffected and only fixes the reference against which it is evaluated; exact knowledge of α_i on the radar side is moreover conservative, in that parameter ignorance would only enlarge the prediction error. The effect of α_i mismatch, with adaptive or IMM estimation, is left to future work.*

Under Assumption 3, the filtering model employed by the radar systems for tracking a gliding vehicle can be formulated in the Earth-fixed coordinate system as follows:

$$\begin{cases} \dot{r}_{\mathrm{H},x} = V_{\mathrm{H},x}, \\ \dot{V}_{\mathrm{H},x} = a_{\mathrm{H},x}, \\ \dot{a}_{\mathrm{H},x} = -\alpha_x a_{\mathrm{H},x} + \omega_x, \\ \dot{r}_{\mathrm{H},y} = V_{\mathrm{H},y}, \\ \dot{V}_{\mathrm{H},y} = a_{\mathrm{H},y}, \\ \dot{a}_{\mathrm{H},y} = -\alpha_y a_{\mathrm{H},y} + \omega_y, \\ \dot{r}_{\mathrm{H},z} = V_{\mathrm{H},z}, \\ \dot{V}_{\mathrm{H},z} = a_{\mathrm{H},z}, \\ \dot{a}_{\mathrm{H},z} = -\alpha_z a_{\mathrm{H},z} + \omega_z, \end{cases} \tag{2}$$

where $r_{\mathrm{H},x}$, $r_{\mathrm{H},y}$, and $r_{\mathrm{H},z}$ denote the position components of the gliding vehicle; $V_{\mathrm{H},x}$, $V_{\mathrm{H},y}$, and $V_{\mathrm{H},z}$ denote the velocity components; $a_{\mathrm{H},x}$, $a_{\mathrm{H},y}$, and $a_{\mathrm{H},z}$ denote the acceleration components along the respective coordinate axes.

Let $\boldsymbol{x}_S(t) = [r_{\mathrm{H},x}, V_{\mathrm{H},x}, a_{\mathrm{H},x}, r_{\mathrm{H},y}, V_{\mathrm{H},y}, a_{\mathrm{H},y}, r_{\mathrm{H},z}, V_{\mathrm{H},z}, a_{\mathrm{H},z}]^\mathrm{T}$, where $\boldsymbol{x}_S(t)$ is the Singer-model state by the radar systems for target tracking. Equation (2) can be rewritten into the standard state-space form as follows:

$$\dot{\boldsymbol{x}}_S(t) = \boldsymbol{A}_S \boldsymbol{x}_S(t) + \boldsymbol{B}_S \boldsymbol{\omega}(t), \tag{3}$$

where

$$\boldsymbol{A}_S = \begin{bmatrix} \boldsymbol{A}_{Sx} & \boldsymbol{O}_{3\times3} & \boldsymbol{O}_{3\times3} \\ \boldsymbol{O}_{3\times3} & \boldsymbol{A}_{Sy} & \boldsymbol{O}_{3\times3} \\ \boldsymbol{O}_{3\times3} & \boldsymbol{O}_{3\times3} & \boldsymbol{A}_{Sz} \end{bmatrix}, \quad \boldsymbol{B}_S = \begin{bmatrix} \boldsymbol{B}_{Sx} & \boldsymbol{O}_{3\times1} & \boldsymbol{O}_{3\times1} \\ \boldsymbol{O}_{3\times1} & \boldsymbol{B}_{Sy} & \boldsymbol{O}_{3\times1} \\ \boldsymbol{O}_{3\times1} & \boldsymbol{O}_{3\times1} & \boldsymbol{B}_{Sz} \end{bmatrix},$$

$\boldsymbol{A}_{Sx}$, $\boldsymbol{A}_{Sy}$, $\boldsymbol{A}_{Sz}$, $\boldsymbol{B}_{Sx}$, $\boldsymbol{B}_{Sy}$, and $\boldsymbol{B}_{Sz}$ can be explicitly formulated as follows:

$$\boldsymbol{A}_{Sx} = \begin{bmatrix} 0 & 1 & 0 \\ 0 & 0 & 1 \\ 0 & 0 & -\alpha_x \end{bmatrix}, \quad \boldsymbol{A}_{Sy} = \begin{bmatrix} 0 & 1 & 0 \\ 0 & 0 & 1 \\ 0 & 0 & -\alpha_y \end{bmatrix}, \quad \boldsymbol{A}_{Sz} = \begin{bmatrix} 0 & 1 & 0 \\ 0 & 0 & 1 \\ 0 & 0 & -\alpha_z \end{bmatrix},$$

$$\boldsymbol{B}_{Sx} = \boldsymbol{B}_{Sy} = \boldsymbol{B}_{Sz} = \begin{bmatrix} 0 \\ 0 \\ 1 \end{bmatrix}, \quad \boldsymbol{\omega}(t) = [\omega_x, \omega_y, \omega_z]^{\mathrm{T}}.$$

Discretization of the above equation yields the following discrete-time form

$$\boldsymbol{x}_S(k+1) = \overline{\boldsymbol{A}}_S \boldsymbol{x}_S(k) + \overline{\boldsymbol{B}}_S \boldsymbol{w}(k), \tag{4}$$

where $\overline{\boldsymbol{A}}_S$ and $\overline{\boldsymbol{B}}_S$ are given by

$$\overline{\boldsymbol{A}}_S = \boldsymbol{I} + \boldsymbol{A}_S T = \begin{bmatrix} \overline{\boldsymbol{A}}_{Sx} & \boldsymbol{O}_{3\times3} & \boldsymbol{O}_{3\times3} \\ \boldsymbol{O}_{3\times3} & \overline{\boldsymbol{A}}_{Sy} & \boldsymbol{O}_{3\times3} \\ \boldsymbol{O}_{3\times3} & \boldsymbol{O}_{3\times3} & \overline{\boldsymbol{A}}_{Sz} \end{bmatrix},$$

$$\overline{\boldsymbol{B}}_S = \begin{bmatrix} \overline{\boldsymbol{B}}_{Sx} & \boldsymbol{O}_{3\times1} & \boldsymbol{O}_{3\times1} \\ \boldsymbol{O}_{3\times1} & \overline{\boldsymbol{B}}_{Sy} & \boldsymbol{O}_{3\times1} \\ \boldsymbol{O}_{3\times1} & \boldsymbol{O}_{3\times1} & \overline{\boldsymbol{B}}_{Sz} \end{bmatrix},$$

$\overline{\boldsymbol{A}}_{Sx}, \overline{\boldsymbol{A}}_{Sy}, \overline{\boldsymbol{A}}_{Sz}, \quad \overline{\boldsymbol{B}}_{Sx}, \overline{\boldsymbol{B}}_{Sy}$, and $\overline{\boldsymbol{B}}_{Sz}$ are explicitly given by

$$\overline{\boldsymbol{A}}_{Sx} = \begin{bmatrix} 1 & T & 0 \\ 0 & 1 & T \\ 0 & 0 & 1 - T\alpha_x \end{bmatrix}, \overline{\boldsymbol{A}}_{Sy} = \begin{bmatrix} 1 & T & 0 \\ 0 & 1 & T \\ 0 & 0 & 1 - T\alpha_y \end{bmatrix},$$

$$\overline{\boldsymbol{A}}_{Sz} = \begin{bmatrix} 1 & T & 0 \\ 0 & 1 & T \\ 0 & 0 & 1 - T\alpha_z \end{bmatrix}, \overline{\boldsymbol{B}}_{Sx} = \overline{\boldsymbol{B}}_{Sy} = \overline{\boldsymbol{B}}_{Sz} = \begin{bmatrix} 0 \\ 0 \\ T \end{bmatrix}$$

where T denotes the discretization time step; $\boldsymbol{I}$ denotes the identity matrix.

Definition 1. *Denote $\boldsymbol{Z}(t)$, $\boldsymbol{H}$ and $\boldsymbol{\zeta}$ as the measurement vector, observation function and measurement noise vector. The radar systems can acquire the relative range r_ρ, longitudinal LOS angle q_E^ρ and lateral LOS angle q_A^ρ between the radar systems and the gliding vehicle. The radar systems' measurement equation is defined as*

$$\boldsymbol{Z}(t) = \boldsymbol{H}(\boldsymbol{x}_S(t)) + \boldsymbol{\zeta}(t) = \begin{bmatrix} \sqrt{x_e^2 + y_e^2 + z_e^2} \\ \arctan\left(\frac{y_e}{x_e}\right) \\ \arctan\left(\frac{z_e}{\sqrt{x_e^2 + y_e^2}}\right) \end{bmatrix} + \begin{bmatrix} \zeta_{r_\rho} \\ \zeta_{q_E^\rho} \\ \zeta_{q_A^\rho} \end{bmatrix}, \tag{5}$$

where x_e, y_e, and z_e denote the position components of the gliding vehicle in the radar-fixed coordinate system; ζ_{r_ρ}, $\zeta_{q_E^\rho}$, and $\zeta_{q_A^\rho}$ represent the measurement noises corresponding to the relative range r_ρ, longitudinal LOS angle q_E^ρ and lateral LOS angle q_A^ρ, respectively.

Relative motion states between the gliding vehicle and radar are derived by constructing the measurement equation using radar systems' measurement data, based on which the maneuver strategy of the gliding vehicle is formulated.

The EKF is adopted to estimate the motion state $\hat{\boldsymbol{x}}_S$ of the gliding vehicle.

$$\begin{cases} \hat{\boldsymbol{x}}_S(k+1|k) = \overline{\boldsymbol{A}}_S \hat{\boldsymbol{x}}_S(k), \\ \hat{\boldsymbol{x}}_S(k+1) = \hat{\boldsymbol{x}}_S(k+1|k) + \boldsymbol{K}_{k+1}\left[\boldsymbol{Z}(k+1) - \boldsymbol{H}_{k+1}\hat{\boldsymbol{x}}_S(k+1|k)\right], \\ \boldsymbol{P}_{k+1|k} = \boldsymbol{\Phi}_{k+1|k}\boldsymbol{P}_{k|k}\boldsymbol{\Phi}_{k+1|k}^{\mathrm{T}} + \boldsymbol{Q}_k, \\ \boldsymbol{K}_{k+1} = \boldsymbol{P}_{k+1|k}\boldsymbol{H}_{k+1}^{\mathrm{T}}\boldsymbol{S}_{k+1}^{-1}, \\ \boldsymbol{P}_{k+1|k+1} = \left(\boldsymbol{I} - \boldsymbol{K}_{k+1}\boldsymbol{H}_{k+1}\right)\boldsymbol{P}_{k+1|k}\left(\boldsymbol{I} - \boldsymbol{K}_{k+1}\boldsymbol{H}_{k+1}\right)^{\mathrm{T}} + \boldsymbol{K}_{k+1}\boldsymbol{R}_{k+1}\boldsymbol{K}_{k+1}^{\mathrm{T}}, \end{cases} \tag{6}$$

where $\boldsymbol{K}$, $\boldsymbol{P}$ and $\boldsymbol{\Phi}$ denote the Kalman gain, covariance matrix and state transition matrix; $\boldsymbol{R}_{k+1}$ and $\boldsymbol{Q}_k$ denote the covariance matrices of measurement noise and system process noise.

$$\boldsymbol{S}_{k+1} = \boldsymbol{R}_{k+1} + \overline{\boldsymbol{H}}_{k+1}\boldsymbol{P}_{k+1|k}\overline{\boldsymbol{H}}_{k+1}^{T}, \quad \overline{\boldsymbol{H}}_{k+1} = \left.\frac{\partial \boldsymbol{h}}{\partial \boldsymbol{x}}\right|_{\hat{\boldsymbol{x}}_{k+1|k}},$$

where $\overline{\boldsymbol{H}}_{k+1}$ denotes the measurement matrix obtained via first-order Taylor linear approximation.

The radar systems predict the position of the gliding vehicle from time t to $t + t_p$ based on the state estimate at time t. Suppose t is the state update time step. Then the number of state updates over the prediction interval from t to $t + t_p$ is $N_p = t_p/T$. Accordingly, the state prediction from time t to $t + t_p$ can be formulated as follows:

$$\hat{\boldsymbol{x}}_S(k+N_p) = \left(\overline{\boldsymbol{A}}_S\right)^{N_p}\hat{\boldsymbol{x}}_S(k) + \left(\overline{\boldsymbol{B}}_S \sum_{k=0}^{N_p-1}\left(\overline{\boldsymbol{A}}_S\right)^{k}\right)\boldsymbol{\omega}(k). \tag{7}$$

The assumptions related to the linearization of the nonlinear functions belong to the solution procedure rather than to the radar model, and are collected as Assumption 4 at the beginning of Section 3.

2.2. Model of Gliding Vehicle Maneuver

Considering the position estimation and trajectory prediction process of the gliding vehicle implemented by the radar systems, the state variables are defined as follows:

$$\boldsymbol{x} = \begin{bmatrix} r_{\mathrm{H},x} & r_{\mathrm{H},y} & r_{\mathrm{H},z} & V_{\mathrm{H}} & \theta_{\mathrm{H}} & \psi_{\mathrm{H}} & \sigma_{\mathrm{H}} \end{bmatrix}^{T}.$$

On this basis, the maneuver model for the gliding phase of the gliding vehicle can be formulated as follows:

$$\begin{cases} \dot{r}_{\mathrm{H},x} = V_{\mathrm{H}}\cos\theta_{\mathrm{H}}\cos\psi_{\mathrm{H}}, \\ \dot{r}_{\mathrm{H},y} = V_{\mathrm{H}}\sin\theta_{\mathrm{H}}, \\ \dot{r}_{\mathrm{H},z} = -V_{\mathrm{H}}\cos\theta_{\mathrm{H}}\sin\psi_{\mathrm{H}}, \\ \dot{V}_{\mathrm{H}} = \dfrac{-X_{\mathrm{H}} - m_{\mathrm{H}}g_0\sin\theta_{\mathrm{H}}}{m_{\mathrm{H}}}, \\ \dot{\theta}_{\mathrm{H}} = \dfrac{Y_{\mathrm{H}}\cos\sigma_{\mathrm{H}} - m_{\mathrm{H}}g_0\cos\theta_{\mathrm{H}}}{m_{\mathrm{H}}V_{\mathrm{H}}}, \\ \dot{\psi}_{\mathrm{H}} = \dfrac{-Y_{\mathrm{H}}\sin\sigma_{\mathrm{H}}}{m_{\mathrm{H}}V_{\mathrm{H}}\cos\theta_{\mathrm{H}}}, \\ \dot{\sigma}_{\mathrm{H}} = u\dot{\sigma}_{\mathrm{H,max}}, \end{cases} \tag{8}$$

where θ_{H} and ψ_{H} denote the trajectory inclination angle and trajectory azimuth angle of the gliding vehicle; X_{H} and Y_{H} denote the aerodynamic drag and aerodynamic lift; m_{H} is the vehicle mass; g_0 denotes the Earth's gravitational acceleration; σ_{H} and $\dot{\sigma}_{\mathrm{H,max}}$ denote the bank angle and its maximum angular rate; and u denotes the control input of the dynamic model.

In this dynamic model, the aerodynamic drag and lift satisfy $X_{\mathrm{H}} = C_{\mathrm{D}}\rho_{\mathrm{H}}V_{\mathrm{H}}^2 S_{\mathrm{H},ref}/2$ and $Y_{\mathrm{H}} = C_{\mathrm{L}}\rho_{\mathrm{H}}V_{\mathrm{H}}^2 S_{\mathrm{H},ref}/2$, where ρ_{H} and $S_{\mathrm{H},ref}$ denote the atmospheric density and the reference area of the gliding vehicle. The aerodynamic coefficients C_{D} and C_{L} are functions of the angle of attack and the Mach number, following the formulation in [14], and are interpolated from the aerodynamic database of the gliding vehicle, which covers $Ma \in [15, 22]$, $\alpha_{\mathrm{H}} \in [0^\circ, 20^\circ]$ and $r_{\mathrm{H},y} \in [20, 60]$km.

The control input u, bank angle σ_{H}, and bank angle rate $\dot{\sigma}_{\mathrm{H}}$ satisfy the following constraint conditions, respectively:

$$\begin{cases} |u| \le 1, \\ |\sigma_{\mathrm{H}}| \le \sigma_{\mathrm{H,max}}, \\ |\dot{\sigma}_{\mathrm{H}}| \le \dot{\sigma}_{\mathrm{H,max}}. \end{cases} \tag{9}$$

To satisfy path constraints such as heat flux, dynamic pressure, and aerodynamic load, ensure flight safety, reduce online computational burden, and improve the real-time performance of the guidance and control system, the angle-of-attack α_{H} profile during the gliding phase of the gliding vehicle is designed as a predefined piecewise function.

$$\alpha_{\mathrm{H}}(V_{\mathrm{H}}) = \begin{cases} \alpha_{\mathrm{H},1}, & V_{\mathrm{H}} \ge V_{\mathrm{H},1}, \\ \alpha_{\mathrm{H},2} + \dfrac{\alpha_{\mathrm{H},1} - \alpha_{\mathrm{H},2}}{V_{\mathrm{H},1} - V_{\mathrm{H},2}}(V_{\mathrm{H}} - V_{\mathrm{H},2}), & V_{\mathrm{H},2} < V_{\mathrm{H}} < V_{\mathrm{H},1}, \\ \alpha_{\mathrm{H},2}, & V_{\mathrm{H}} \le V_{\mathrm{H},2}, \end{cases} \tag{10}$$

where $\alpha_{\mathrm{H},1}$ and $\alpha_{\mathrm{H},2}$ denote the upper and lower bounds of the angle-of-attack threshold; $V_{\mathrm{H},1}$ and $V_{\mathrm{H},2}$ denote the velocity thresholds separating the high-speed and transition phases, and the transition and low-speed phases.

The atmospheric density ρ_{H} required for calculating the aerodynamic forces of the vehicle is determined by the following exponential atmospheric model.

$$\rho_{\mathrm{H}} = \rho_{\mathrm{H},0} e^{-\beta r_{\mathrm{H},y}}, \tag{11}$$

where $\rho_{\mathrm{H},0} = 1.225\,\mathrm{kg}\cdot\mathrm{m}^{-3}$ denotes the sea-level atmospheric density, and $\beta = 1/7110\ \mathrm{m}^{-1}$ is the atmospheric attenuation constant.

Since the angle of attack is predefined as a preset piecewise function with respect to velocity, the bank angle σ, governed by the control input u, is the sole control variable to be regulated.

Meanwhile, gliding vehicle is mainly subjected to the following process constraints during the gliding maneuver phase.

$$\begin{cases} \dot{Q}_{\mathrm{H}} = k_{\mathrm{Q}}\rho_{\mathrm{H}}^{k_1} V_{\mathrm{H}}^{k_2} \le \dot{Q}_{\mathrm{H,max}}, \\ q_{\mathrm{H}} = \dfrac{\rho_{\mathrm{H}} V_{\mathrm{H}}^2}{2} \le q_{\mathrm{H,max}}, \\ n_{\mathrm{H}} = \dfrac{\sqrt{Y_{\mathrm{H}}^2 + X_{\mathrm{H}}^2}}{m_{\mathrm{H}} g_0} \le n_{\mathrm{H,max}}, \end{cases} \tag{12}$$

where $\dot{Q}_{\mathrm{H}}$, q_{H}, n_{H} denote the heat flux, dynamic pressure and aerodynamic overload; $\dot{Q}_{\mathrm{H,max}}$, $q_{\mathrm{H,max}}$, $n_{\mathrm{H,max}}$ denote the constraint limits of heat flux, dynamic pressure and aerodynamic overload, respectively; k_{Q},k_1, k_2 denote constant parameters.

The flight dynamics in Equation (8) are affected by three elements of different nature, which are treated separately in what follows. The first is dynamic uncertainty, arising from unmodeled dynamics and parameter perturbations. Mathematically, it enters the

translational dynamics as an additive perturbation term superimposed on the nominal dynamics, and its magnitude is bounded rather than known in advance. The second is random noise, which in this paper does not act on the vehicle dynamics but on the radar tracking loop: the Singer acceleration model in Equations (1)–(3) is driven by zero-mean white Gaussian noise, and the measurements in Equation (5) are corrupted by zero-mean measurement noise, the statistics of both being characterized by the process and measurement covariance matrices in Equation (6). The third is the set of process constraints in Equation (12), namely the heat flux, dynamic pressure and aerodynamic overload limits, which are deterministic inequalities that any admissible trajectory must satisfy.

These elements play different roles and are therefore coupled in a specific manner. The dynamic perturbation generates an uncertainty set: owing to the perturbation, the state trajectory is no longer a single deterministic curve but a family of admissible realizations, each corresponding to one admissible value of the perturbation. The process constraints must hold simultaneously for every member of this family, i.e., for all admissible perturbation values and not merely along the nominal trajectory. This requirement, that deterministic flight constraints be enforced over the entire uncertainty set generated by the bounded dynamic perturbation, is referred to in this paper as the uncertain dynamic constraint. The random noise, by contrast, neither enlarges this uncertainty set nor enters the maneuver optimization: it acts on the radar measurement and filtering process and thus determines the estimation and prediction accuracy against which the maneuver is evaluated, so that it shapes the cost function rather than the feasible set.

Only bounded uncertainty is considered: the perturbation is assumed to be bounded in magnitude, no probability distribution is assumed for it, and no probabilistic or chance constraint is adopted. The uncertain dynamic constraints are therefore treated in a deterministic, bounded-error sense.

This paper addresses the following three problems:

1. how to realize the incremental transformation of nonlinear systems and derive error bounds for the transformed models;
2. how to realize the quantitative analysis of maneuver strategy effectiveness;
3. how to solve the problem of online optimal maneuver with complex constraints.

3. Main Results

The proposed maneuver strategy is decomposed into two core problems in this section: the problem of incremental formulation for nonlinear systems, and the problem of designing maneuver strategies for maximizing radar prediction errors. First, the nonlinear flight dynamics are transformed into a weakly model-dependent incremental linear system with the linearization error bounded. Next, the incremental linear system is discretized to derive the discrete-time incremental linear system. Afterwards, a cost function is designed and multiple nonlinear flight constraints are correspondingly transformed into incremental state constraints. Finally, an IMPC-based algorithm is introduced to facilitate the implementation of the proposed maneuver strategy.

Assumption 4. *The following first-order approximations are adopted: (1) Equation (5) is linearized about the one-step prediction $\hat{x}_S(k+1|k)$ in the EKF, with terms of second and higher order neglected, the LOS angles kept away from the singular directions and unwrapped before differencing; (2) the third, sixth, ninth and twelfth equations of Equation (18) are expanded about (x_0, u_0), with the state-variation terms insensitive to Δu neglected, the sampling frequency being high enough for the discarded residual to satisfy Equation (29) with $c_b < 1$; (3) the process constraints in Equation (12) are expanded about $V_{\mathrm{H},0}$, the velocity variation within one control update being small compared with $V_{\mathrm{H},0}$.*

Remark 4. *Approximation (1) affects the estimate produced by the radar and hence the value of the index, but it is present identically in the IMPC maneuver and constant control cases and therefore does not bias the comparison of Section 4. Approximation (2) underlies the weak model dependence of the proposed method: the discarded residual is bounded by Equation (29), and Figure 11 shows that the closed-loop prediction error of the incremental model stays within* 25 m, *about* 2% *of the peak, of the nonlinear reference. Approximation (3) is verified by re-evaluating the nonlinear constraints on the propagated trajectory (Figure 7) and by the backtracking test of Section 3.2.2*

3.1. Incremental Linear System

3.1.1. Weak Model-Dependent Incremental Linear System

The TSS principle [36], also known as singular perturbation theory, describes the inherent multi-time-scale characteristics of nonlinear dynamic systems arising from singular perturbations. Based on the TSS principle, flight vehicle dynamics can be decoupled into fast and slow subsystems for separate linearization, which considerably mitigates linear approximation errors.

Based on the TSS principle, system state variables are sorted into fast and slow states. The variables θ_{H}, ψ_{H} and σ_{H} are directly or indirectly driven by control inputs and hence treated as fast states, while $r_{\mathrm{H},x}$, $r_{\mathrm{H},y}$, $r_{\mathrm{H},z}$ and V_{H} evolve under the impacts of θ_{H} and ψ_{H} and are categorized as slow states. Following the above analysis, incremental linearization is performed for the original nonlinear system.

Let $\boldsymbol{x}_{r,x1} = r_{\mathrm{H},x}$. By continuously differentiating $\boldsymbol{x}_{r,x1}$ three times, the nonaffine nonlinear system is transformed into an affine nonlinear system. The resulting third-order system can be expressed as follows:

$$\begin{cases} \dot{\boldsymbol{x}}_{r,x1} &= \boldsymbol{x}_{r,x2}, \\ \dot{\boldsymbol{x}}_{r,x2} &= \boldsymbol{x}_{r,x3}, \\ \dot{\boldsymbol{x}}_{r,x3} &= \boldsymbol{f}_{r,x}(\boldsymbol{x}) + \boldsymbol{g}_{r,x}(\boldsymbol{x})\,\boldsymbol{u}, \end{cases} \tag{13}$$

where $\boldsymbol{f}_{r,x}(\boldsymbol{x})$ and $\boldsymbol{g}_{r,x}(\boldsymbol{x})$ are given by

$$\begin{aligned} \boldsymbol{f}_{r,x}(\boldsymbol{x}) = {} & -g_0\dot{\theta}_{\mathrm{H}}(\cos\theta_{\mathrm{H}})^2\cos\psi_{\mathrm{H}} - 2\dot{V}_{\mathrm{H}}\dot{\theta}_{\mathrm{H}}\sin\theta_{\mathrm{H}}\cos\psi_{\mathrm{H}} - \dot{V}_{\mathrm{H}}\dot{\psi}_{\mathrm{H}}\cos\theta_{\mathrm{H}}\sin\psi_{\mathrm{H}} - \\ & - V_{\mathrm{H}}\cos\theta_{\mathrm{H}}\cos\psi_{\mathrm{H}}(\dot{\theta}_{\mathrm{H}})^2 + V_{\mathrm{H}}\sin\theta_{\mathrm{H}}\sin\psi_{\mathrm{H}}\dot{\psi}_{\mathrm{H}}\dot{\theta}_{\mathrm{H}} - \\ & - g_0(\sin\theta_{\mathrm{H}})^2\cos\psi_{\mathrm{H}} + \frac{V_{\mathrm{H}}\dot{\psi}_{\mathrm{H}}\cos\psi_{\mathrm{H}}\sin\sigma_{\mathrm{H}}}{m_{\mathrm{H}}}, \end{aligned}$$

$$\boldsymbol{g}_{r,x}(\boldsymbol{x}) = \frac{V_{\mathrm{H}}\dot{\sigma}_{\mathrm{H,max}}\sin\theta_{\mathrm{H}}\cos\psi_{\mathrm{H}}\sin\sigma_{\mathrm{H}}}{m_{\mathrm{H}}} + \frac{V_{\mathrm{H}}\dot{\sigma}_{\mathrm{H,max}}\sin\psi_{\mathrm{H}}\cos\sigma_{\mathrm{H}}}{m_{\mathrm{H}}}.$$

Remark 5. *Continuous differentiation is performed on the state variable $r_{\mathrm{H},x}$ to transform the non-affine nonlinear system into an affine nonlinear system. On this basis, the incremental approach is adopted to further convert it into an incremental linear dynamic system [25]. In the subsequent methodology, the controller is designed to regulate the positional components of a hypersonic vehicle. To simplify the derivation process, incremental processing is no longer implemented for the state variables θ_{H}, ψ_{H} and σ_{H}. As the sampling frequency increases, the linearization error decreases significantly and can be regarded as bounded [37]. Accordingly, the influence of such error is neglected in the subsequent derivation.*

Similarly, let $\boldsymbol{x}_{r,x1} = r_{\mathrm{H},y}$ and $\boldsymbol{x}_{r,x1} = r_{\mathrm{H},z}$. The third-order differential systems corresponding to $r_{\mathrm{H},y}$ and $r_{\mathrm{H},z}$ can be derived.

$$\begin{cases} \dot{\boldsymbol{x}}_{r,y1} &= \boldsymbol{x}_{r,y2}, \\ \dot{\boldsymbol{x}}_{r,y2} &= \boldsymbol{x}_{r,y3}, \\ \dot{\boldsymbol{x}}_{r,y3} &= \boldsymbol{f}_{r,y}(\boldsymbol{x}) + \boldsymbol{g}_{r,y}(\boldsymbol{x})\,\boldsymbol{u}, \end{cases} \tag{14}$$

$$\begin{cases} \dot{\boldsymbol{x}}_{r,z1} &= \boldsymbol{x}_{r,z2}, \\ \dot{\boldsymbol{x}}_{r,z2} &= \boldsymbol{x}_{r,z3}, \\ \dot{\boldsymbol{x}}_{r,z3} &= \boldsymbol{f}_{r,z}(\boldsymbol{x}) + \boldsymbol{g}_{r,z}(\boldsymbol{x})\,\boldsymbol{u}, \end{cases} \tag{15}$$

where $\boldsymbol{f}_{r,y}(\boldsymbol{x})$, $\boldsymbol{g}_{r,y}(\boldsymbol{x})$, $\boldsymbol{f}_{r,z}(\boldsymbol{x})$, and $\boldsymbol{g}_{r,z}(\boldsymbol{x})$ are expressed as follows:

$$\boldsymbol{f}_{r,y}(\boldsymbol{x}) = -g_0\dot{\theta}_{\mathrm{H}}\cos\theta_{\mathrm{H}}\sin\theta_{\mathrm{H}} + 2\dot{V}_{\mathrm{H}}\dot{\theta}_{\mathrm{H}}\cos\theta_{\mathrm{H}} - V_{\mathrm{H}}\sin\theta_{\mathrm{H}}\left(\dot{\theta}_{\mathrm{H}}\right)^2 - g_0\dot{\theta}_{\mathrm{H}}\cos\theta_{\mathrm{H}}\sin\theta_{\mathrm{H}},$$

$$\boldsymbol{g}_{r,y}(\boldsymbol{x}) = -\frac{Y_{\mathrm{H}}\dot{\sigma}_{\mathrm{H,max}}\cos\theta_{\mathrm{H}}\sin\sigma_{\mathrm{H}}}{m_{\mathrm{H}}},$$

$$\begin{aligned} \boldsymbol{f}_{r,z}(\boldsymbol{x}) = {} & g_0\dot{\theta}_{\mathrm{H}}(\cos\theta_{\mathrm{H}})^2\sin\psi_{\mathrm{H}} + 2\dot{V}_{\mathrm{H}}\dot{\theta}_{\mathrm{H}}\sin\theta_{\mathrm{H}}\sin\psi_{\mathrm{H}} - \dot{V}_{\mathrm{H}}\dot{\psi}_{\mathrm{H}}\cos\theta_{\mathrm{H}}\cos\psi_{\mathrm{H}} \\ & + V_{\mathrm{H}}\cos\theta_{\mathrm{H}}\sin\psi_{\mathrm{H}}\left(\dot{\theta}_{\mathrm{H}}\right)^2 + V_{\mathrm{H}}\sin\theta_{\mathrm{H}}\cos\psi_{\mathrm{H}}\dot{\psi}_{\mathrm{H}}\dot{\theta}_{\mathrm{H}} \\ & - g_0\dot{\theta}_{\mathrm{H}}(\sin\theta_{\mathrm{H}})^2\sin\psi_{\mathrm{H}} - \frac{Y_{\mathrm{H}}\dot{\psi}_{\mathrm{H}}\sin\psi_{\mathrm{H}}\sin\sigma_{\mathrm{H}}}{m_{\mathrm{H}}}, \end{aligned}$$

$$\boldsymbol{g}_{r,z}(\boldsymbol{x}) = -\frac{Y_{\mathrm{H}}\dot{\sigma}_{\mathrm{H,max}}\sin\theta_{\mathrm{H}}\sin\psi_{\mathrm{H}}\sin\sigma_{\mathrm{H}}}{m_{\mathrm{H}}} + \frac{Y_{\mathrm{H}}\dot{\sigma}_{\mathrm{H,max}}\cos\psi_{\mathrm{H}}\cos\sigma_{\mathrm{H}}}{m_{\mathrm{H}}}.$$

Let $\boldsymbol{x}_{V1} = V_{\mathrm{H}}$; continuous differentiation of the state variable $\boldsymbol{x}_{V1}$ can yield

$$\begin{cases} \dot{\boldsymbol{x}}_{V1} &= \boldsymbol{x}_{V2}, \\ \dot{\boldsymbol{x}}_{V2} &= \boldsymbol{x}_{V3}, \\ \dot{\boldsymbol{x}}_{V3} &= \boldsymbol{f}_{V}(\boldsymbol{x}) + \boldsymbol{g}_{V}(\boldsymbol{x})\,\boldsymbol{u}, \end{cases} \tag{16}$$

where $\boldsymbol{f}_V(\boldsymbol{x})$ and $\boldsymbol{g}_V(\boldsymbol{x})$ are respectively expressed as

$$\boldsymbol{f}_V(\boldsymbol{x}) = g_0\sin\theta_{\mathrm{H}}\left(\dot{\theta}_{\mathrm{H}}\right)^2 - \frac{g_0^2\dot{\theta}_{\mathrm{H}}\cos\theta_{\mathrm{H}}\sin\theta_{\mathrm{H}}}{V_{\mathrm{H}}} + \frac{Y_{\mathrm{H}}g_0\cos\theta_{\mathrm{H}}\cos\sigma_{\mathrm{H}}}{m_{\mathrm{H}}V_{\mathrm{H}}^2} - \frac{g_0^2(\cos\theta_{\mathrm{H}})^2}{V_{\mathrm{H}}},$$

$$\boldsymbol{g}_V(\boldsymbol{x}) = \frac{Y_{\mathrm{H}}\dot{\sigma}_{\mathrm{H,max}}g_0\cos\theta_{\mathrm{H}}\sin\sigma_{\mathrm{H}}}{m_{\mathrm{H}}V_{\mathrm{H}}}.$$

Redefine the state variables of the system as

$$\boldsymbol{x}_A = \begin{bmatrix} \boldsymbol{x}_{r,x} & \boldsymbol{x}_{r,y} & \boldsymbol{x}_{r,z} & \boldsymbol{x}_V \end{bmatrix}^{\mathrm{T}}, \tag{17}$$

where $\boldsymbol{x}_{r,x}$, $\boldsymbol{x}_{r,y}$, $\boldsymbol{x}_{r,z}$ and $\boldsymbol{x}_{r,V}$ are respectively expressed as follows:

$$\begin{cases} \boldsymbol{x}_{r,x} = [\boldsymbol{x}_{r,x1},\ \boldsymbol{x}_{r,x2},\ \boldsymbol{x}_{r,x3}]^{\mathrm{T}}, \\ \boldsymbol{x}_{r,y} = [\boldsymbol{x}_{r,y1},\ \boldsymbol{x}_{r,y2},\ \boldsymbol{x}_{r,y3}]^{\mathrm{T}}, \\ \boldsymbol{x}_{r,z} = [\boldsymbol{x}_{r,z1},\ \boldsymbol{x}_{r,z2},\ \boldsymbol{x}_{r,z3}]^{\mathrm{T}}, \\ \boldsymbol{x}_{r,V} = [\boldsymbol{x}_{r,V1},\ \boldsymbol{x}_{r,V2},\ \boldsymbol{x}_{r,V3}]^{\mathrm{T}}. \end{cases}$$

Therefore, the maneuver dynamic model of the gliding vehicle can be formulated as

$$\begin{cases} \dot{\boldsymbol{x}}_{r,x1} &= \boldsymbol{x}_{r,x2}, \\ \dot{\boldsymbol{x}}_{r,x2} &= \boldsymbol{x}_{r,x3}, \\ \dot{\boldsymbol{x}}_{r,x3} &= \boldsymbol{f}_{r,x}(\boldsymbol{x}) + \boldsymbol{g}_{r,x}(\boldsymbol{x})\, u, \\ \dot{\boldsymbol{x}}_{r,y1} &= \boldsymbol{x}_{r,y2}, \\ \dot{\boldsymbol{x}}_{r,y2} &= \boldsymbol{x}_{r,y3}, \\ \dot{\boldsymbol{x}}_{r,y3} &= \boldsymbol{f}_{r,y}(\boldsymbol{x}) + \boldsymbol{g}_{r,y}(\boldsymbol{x})\, u, \\ \dot{\boldsymbol{x}}_{r,z1} &= \boldsymbol{x}_{r,z2}, \\ \dot{\boldsymbol{x}}_{r,z2} &= \boldsymbol{x}_{r,z3}, \\ \dot{\boldsymbol{x}}_{r,z3} &= \boldsymbol{f}_{r,z}(\boldsymbol{x}) + \boldsymbol{g}_{r,z}(\boldsymbol{x})\, u, \\ \dot{\boldsymbol{x}}_{V1} &= \boldsymbol{x}_{V2}, \\ \dot{\boldsymbol{x}}_{V2} &= \boldsymbol{x}_{V3}, \\ \dot{\boldsymbol{x}}_{V3} &= \boldsymbol{f}_{V}(\boldsymbol{x}) + \boldsymbol{g}_{V}(\boldsymbol{x})\, u. \end{cases} \tag{18}$$

Remark 6. *Based on the TSS principle and the incremental linearization process [38,39], after the first-order Taylor expansion is performed on the third, sixth, ninth, and twelfth terms of the nonlinear system (18) and the state change terms that are insensitive to control input variations are neglected [40,41], an approximate incremental linear dynamic system can be derived as*

$$\dot{\boldsymbol{x}}_{r,x3} = \dot{\boldsymbol{x}}_{r,x3,0} + \boldsymbol{g}_{r,x}(x_0)\Delta\boldsymbol{u}, \tag{19}$$

$$\dot{\boldsymbol{x}}_{r,y3} = \dot{\boldsymbol{x}}_{r,y3,0} + \boldsymbol{g}_{r,y}(x_0)\Delta\boldsymbol{u}, \tag{20}$$

$$\dot{\boldsymbol{x}}_{r,z3} = \dot{\boldsymbol{x}}_{r,z3,0} + \boldsymbol{g}_{r,z}(x_0)\Delta\boldsymbol{u}, \tag{21}$$

$$\dot{\boldsymbol{x}}_{V3} = \dot{\boldsymbol{x}}_{V3,0} + \boldsymbol{g}_{V}(x_0)\Delta\boldsymbol{u}, \tag{22}$$

where $\Delta\boldsymbol{u} = \boldsymbol{u} - \boldsymbol{u}_0$ *denotes the incremental control signal of the entire system.*

Remark 7. *Through the above incremental linearization procedure, the nonlinear system described by Equation (8) is converted into a weakly model-dependent incremental linearized dynamic system. Such low model dependence stems from its independence of the function term* $\boldsymbol{f}(\boldsymbol{x})$ *in the original nonlinear system, which indicates that the control signals are nearly insensitive to the specific system model. More precisely, the model information contained in* $\boldsymbol{f}(\boldsymbol{x})$ *can be substituted via online monitoring of* $\dot{\boldsymbol{x}}_0$*. Consequently, the effectiveness of the controller designed based on this scheme is determined by the sensor measurement process.*

Due to unmodeled dynamics and uncertain disturbances, $\boldsymbol{g}_{r,x}(x_0)$, $\boldsymbol{g}_{r,y}(x_0)$, $\boldsymbol{g}_{r,z}(x_0)$ and $\boldsymbol{g}_{V}(x_0)$ suffer from inherent inaccuracies. Accordingly, such inaccuracies of the four functions are fully accounted for in the subsequent derivation.

3.1.2. Error Bounds of the Incremental Linear System

For the nonlinear system $\dot{\boldsymbol{x}}_{r,x3} = \boldsymbol{f}_{r,x}(\boldsymbol{x}) + \boldsymbol{g}_{r,x}(\boldsymbol{x})u$, it can be approximated by the estimated functions $\hat{\boldsymbol{f}}_{r,x}(x)$ and $\hat{\boldsymbol{g}}_{r,x}(x)$, and the approximate system is expressed as

$$\dot{\hat{\boldsymbol{x}}}_{r,x3} = \hat{\boldsymbol{f}}_{r,x}(x) + \hat{\boldsymbol{g}}_{r,x}(x)\boldsymbol{u}. \tag{23}$$

The mismatch error $\boldsymbol{\xi}_{\dot{x}}$ between the approximate system and the nominal system is defined as

$$\begin{aligned} \boldsymbol{\xi}_{\dot{x}} &= \dot{\boldsymbol{x}}_{r,x3} - \dot{\hat{\boldsymbol{x}}}_{r,x3} \\ &= \boldsymbol{f}_{r,x}(\boldsymbol{x}) + \boldsymbol{g}_{r,x}(\boldsymbol{x})\boldsymbol{u} - \hat{\boldsymbol{f}}_{r,x}(\boldsymbol{x}) - \hat{\boldsymbol{g}}_{r,x}(\boldsymbol{x})\boldsymbol{u} \\ &= \left(\boldsymbol{f}_{r,x}(\boldsymbol{x}) - \hat{\boldsymbol{f}}_{r,x}(\boldsymbol{x})\right) + \left(\boldsymbol{g}_{r,x}(\boldsymbol{x}) - \hat{\boldsymbol{g}}_{r,x}(\boldsymbol{x})\right)\boldsymbol{u}. \end{aligned} \tag{24}$$

An approximate incremental linear dynamic system is derived by introducing a constant matrix $\hat{\boldsymbol{G}}_{r,x}$

$$\hat{\dot{\boldsymbol{x}}}_{r,x3} = \dot{\boldsymbol{x}}_{r,x3,0} + \hat{\boldsymbol{G}}_{r,x}\Delta\boldsymbol{u}. \tag{25}$$

Then the mismatch error between the approximate incremental linear dynamic system and the nonlinear nominal system is given by

$$\begin{aligned}\boldsymbol{\xi}_{r,x} &= \dot{\boldsymbol{x}}_{r,x3} - \hat{\dot{\boldsymbol{x}}}_{r,x3} \\ &= \boldsymbol{f}_{r,x}(\boldsymbol{x}) + \boldsymbol{g}_{r,x}(\boldsymbol{x})\boldsymbol{u} - \dot{\boldsymbol{x}}_{r,x3,0} - \hat{\boldsymbol{G}}_{r,x}\Delta\boldsymbol{u} \\ &= \boldsymbol{f}_{r,x}(\boldsymbol{x}) + \boldsymbol{g}_{r,x}(\boldsymbol{x})\boldsymbol{u} - \boldsymbol{f}_{r,x}(x_0) - \boldsymbol{g}_{r,x}(x_0)u_0 - \hat{\boldsymbol{G}}_{r,x}\Delta\boldsymbol{u} \\ &= \left(\boldsymbol{g}_{r,x}(\boldsymbol{x}) - \hat{\boldsymbol{G}}_{r,x}\right)\Delta\boldsymbol{u} + \boldsymbol{\delta}_{\Delta u_0},\end{aligned} \tag{26}$$

where $\boldsymbol{\delta}_{\Delta u_0}$ is given by

$$\boldsymbol{\delta}_{\Delta u_0} = \left(\hat{\boldsymbol{f}}_{r,x}(x) - \boldsymbol{f}_{r,x}(x_0)\right) + \left[\left(\boldsymbol{g}_{r,x}(\boldsymbol{x}) - \hat{\boldsymbol{G}}_{r,x}\right) - \left(\boldsymbol{g}_{r,x}(x_0) - \hat{\boldsymbol{G}}_{r,x}\right)\right]u_0. \tag{27}$$

A sufficiently high sampling frequency ensures that the gap between consecutively sampled state values becomes sufficiently small. Therefore, it can be considered that $\boldsymbol{\delta}_{\Delta u_0}$ satisfies $\exists\overline{\boldsymbol{\delta}}_{\Delta u_0} \in \mathbb{R}^+, \left\|\boldsymbol{\delta}_{\Delta u_0}\right\| \leq \overline{\boldsymbol{\delta}}_{\Delta u_0}$. On this basis, an approximate incremental linear dynamic system considering incremental linear errors can be expressed as

$$\hat{\dot{\boldsymbol{x}}}_{r,x3} = \dot{\boldsymbol{x}}_{r,x3,0} + \hat{\boldsymbol{G}}_{r,x}(\Delta\boldsymbol{u} + \boldsymbol{\xi}_{r,x}). \tag{28}$$

where

$$\boldsymbol{\xi}_{r,x} = \left(\hat{\boldsymbol{G}}_{r,x}^{-1}\boldsymbol{g}_{r,x}(x_0) - I\right)\Delta\boldsymbol{u},$$

denote the incremental linearization error.

Definition 2. *For the incremental linear dynamic system* (28)*, the incremental linearization error is defined as* $\boldsymbol{\xi}_{r,x} = \left(\hat{\boldsymbol{G}}_{r,x}^{-1}\boldsymbol{g}_{r,x}(x_0) - I\right)\Delta\boldsymbol{u}$*. Assume there exists* $\exists\Delta u_{\max} \in \mathbb{R}^+$ *such that* $\|\Delta\boldsymbol{u}\| \leq \Delta u_{\max}$*. By selecting an appropriate input matrix* $\hat{\boldsymbol{G}}_{r,x}$*, the inequality* $\left\|\hat{\boldsymbol{G}}_{r,x}^{-1}\boldsymbol{g}_{r,x}(x_0) - I\right\| \leq c_b < 1$ *holds. Consequently,* $\|\boldsymbol{\xi}_{r,x}\|$ *satisfies*

$$\|\boldsymbol{\xi}_{r,x}\| \leq \left\|\hat{\boldsymbol{G}}_{r,x}^{-1}\boldsymbol{g}_{r,x}(x_{r,x_0}) - \boldsymbol{I}\right\|\|\Delta\boldsymbol{u}\| \leq c_b\Delta u_{\max}, \tag{29}$$

where c_b *is a positive constant less than 1.*

Equation (29) is a single-step bound for one incremental subsystem in open loop. It does not guarantee the robustness of the closed loop. What it shows is that the residual entering each subsystem is bounded, and that this bound can be reduced by a proper choice of $\hat{\boldsymbol{G}}_{r,x}$. The approximation used in the IMPC design therefore does not rely on the accuracy of the nominal nonlinear model.

Remark 8. *The errors in Equations* (24) *and* (26) *come from different sources. The term* $\boldsymbol{\xi}_{\dot{\boldsymbol{x}}}$ *contains the identification errors of both* $\boldsymbol{f}_{r,x}(\boldsymbol{x})$ *and* $\boldsymbol{g}_{r,x}(\boldsymbol{x})$*. The part* $\left(\boldsymbol{f}_{r,x}(\boldsymbol{x}) - \hat{\boldsymbol{f}}_{r,x}(\boldsymbol{x})\right)$ *is added directly to the dynamics, so its size is set by the magnitude of f itself. For the glide dynamics f includes the gravity, aerodynamic and kinematic terms, and a moderate relative error in each of them still gives a large absolute error. The term* $\boldsymbol{\xi}_{r,x}$ *in Equation* (26) *contains no* $\boldsymbol{f}_{r,x}(\boldsymbol{x})$*. The effect of f is replaced by the measured* $\dot{\boldsymbol{x}}_{r,x3,0}$*, and what remains is the error of* $\boldsymbol{g}_{r,x}(\boldsymbol{x})$ *multiplied by the bounded increment* $\Delta\boldsymbol{u}$*, together with* $\boldsymbol{\delta}_{\Delta u_0}$*. The first part depends on how well the constant matrix* $\hat{\boldsymbol{G}}_{r,x}$ *represents* $\boldsymbol{g}_{r,x}(x_0)$*. The second part decreases as the sampling interval is reduced. The incremental residual is therefore governed mainly by the relative error of one gain function, whereas the model-mismatch*

error is governed by the absolute error of the whole dynamics. For the same level of model inaccuracy the former is smaller. This is why the incremental system depends less on the nominal model.

Similarly, with the introduction of constant matrices $\hat{\boldsymbol{G}}_{r,y}$, $\hat{\boldsymbol{G}}_{r,z}$, and $\hat{\boldsymbol{G}}_V$, Equations (20)–(22) can be rewritten as

$$\dot{\boldsymbol{x}}_{r,y3} = \dot{\boldsymbol{x}}_{r,y3,0} + \hat{\boldsymbol{G}}_{r,y}\Delta\boldsymbol{u} + \boldsymbol{\xi}_{r,y}, \tag{30}$$

$$\dot{\boldsymbol{x}}_{r,z3} = \dot{\boldsymbol{x}}_{r,z3,0} + \hat{\boldsymbol{G}}_{r,z}\Delta\boldsymbol{u} + \boldsymbol{\xi}_{r,z}, \tag{31}$$

$$\dot{\boldsymbol{x}}_{V3} = \dot{\boldsymbol{x}}_{V3,0} + \hat{\boldsymbol{G}}_{V}\Delta\boldsymbol{u} + \boldsymbol{\xi}_{V}, \tag{32}$$

where $\boldsymbol{\xi}_{r,y}$, $\boldsymbol{\xi}_{r,z}$, and $\boldsymbol{\xi}_V$ denote the incremental linearization errors.

Based on the above derivation, Equations (13)–(16) can be written in the following form:

$$\begin{cases} \dot{\boldsymbol{x}}_{r,x1} = \boldsymbol{x}_{r,x2}, \\ \dot{\boldsymbol{x}}_{r,x2} = \boldsymbol{x}_{r,x3}, \\ \dot{\boldsymbol{x}}_{r,x3} = \dot{\boldsymbol{x}}_{r,x3,0} + \hat{\boldsymbol{G}}_{r,x}\Delta\boldsymbol{u} + \boldsymbol{\xi}_{r,x}, \end{cases} \tag{33}$$

$$\begin{cases} \dot{\boldsymbol{x}}_{r,y1} = \boldsymbol{x}_{r,y2}, \\ \dot{\boldsymbol{x}}_{r,y2} = \boldsymbol{x}_{r,y3}, \\ \dot{\boldsymbol{x}}_{r,y3} = \dot{\boldsymbol{x}}_{r,y3,0} + \hat{\boldsymbol{G}}_{r,y}\Delta\boldsymbol{u} + \boldsymbol{\xi}_{r,y}, \end{cases} \tag{34}$$

$$\begin{cases} \dot{\boldsymbol{x}}_{r,z1} = \boldsymbol{x}_{r,z2}, \\ \dot{\boldsymbol{x}}_{r,z2} = \boldsymbol{x}_{r,z3}, \\ \dot{\boldsymbol{x}}_{r,z3} = \dot{\boldsymbol{x}}_{r,z3,0} + \hat{\boldsymbol{G}}_{r,z}\Delta\boldsymbol{u} + \boldsymbol{\xi}_{r,z}, \end{cases} \tag{35}$$

$$\begin{cases} \dot{\boldsymbol{x}}_{V1} = \boldsymbol{x}_{V2}, \\ \dot{\boldsymbol{x}}_{V2} = \boldsymbol{x}_{V3}, \\ \dot{\boldsymbol{x}}_{V3} = \dot{\boldsymbol{x}}_{V3,0} + \hat{\boldsymbol{G}}_{V}\Delta\boldsymbol{u} + \boldsymbol{\xi}_{V}. \end{cases} \tag{36}$$

3.1.3. Discrete-Time Incremental Linear Approximation System

By discretizing the incremental system via the Euler numerical differentiation method, an approximate discrete-time incremental linear dynamic system can be obtained.

$$\dot{x}^*(k) = \frac{x^*(k+1) - x^*(k)}{T_s} + \omega^*(k), \tag{37}$$

where $\omega^*(k)$ denotes the discretization error.

Discretizing the incremental linear system in Equation (33) yields a discrete-time incremental linear dynamic system, which is derived via the Euler numerical differentiation scheme.

$$\begin{cases} \boldsymbol{x}_{r,x1}(k+1) = \boldsymbol{x}_{r,x1}(k) + T_s\boldsymbol{x}_{r,x2}(k) - T_s\boldsymbol{\omega}_1(k), \\ \boldsymbol{x}_{r,x2}(k+1) = \boldsymbol{x}_{r,x2}(k) + T_s\boldsymbol{x}_{r,x3}(k) - T_s\boldsymbol{\omega}_2(k), \\ \boldsymbol{x}_{r,x3}(k+1) = 2\boldsymbol{x}_{r,x3}(k) - \boldsymbol{x}_{r,x3}(k-1) + T_s\hat{\boldsymbol{G}}_{r,x}\Delta\boldsymbol{u} + T_s\tilde{\boldsymbol{\varepsilon}}_{r,x} + T_s\overline{\boldsymbol{\omega}}_3(k), \end{cases} \tag{38}$$

where $\tilde{\boldsymbol{\varepsilon}}_{r,x} = \hat{\boldsymbol{G}}_{r,x}\boldsymbol{\xi}_{r,x}$, and $\overline{\boldsymbol{\omega}}_3(k) = \boldsymbol{\omega}_3(k-1) - \boldsymbol{\omega}_3(k)$

Let $\boldsymbol{x}_{r,x}(k) = \begin{bmatrix} \boldsymbol{x}_{r,x1}(k) & \boldsymbol{x}_{r,x2}(k) & \boldsymbol{x}_{r,x3}(k) \end{bmatrix}^{\mathrm{T}}$. Then, Equation (38) can be rewritten as

$$\boldsymbol{x}_{r,x}(k+1) = \boldsymbol{A}_{r,x1}\boldsymbol{x}_{r,x}(k) + \boldsymbol{A}_{r,x2}\boldsymbol{x}_{r,x}(k-1) + \boldsymbol{B}_{r,x1}\Delta\boldsymbol{u}(k) + \boldsymbol{\xi}_{r,x}, \tag{39}$$

where $\boldsymbol{A}_{r,x1}$, $\boldsymbol{A}_{r,x2}$, $\boldsymbol{B}_{r,x1}$, and $\boldsymbol{\xi}_{r,x}$ are respectively given by

$$\boldsymbol{A}_{r,x1} = \begin{bmatrix} \boldsymbol{I} & T_s\boldsymbol{I} & \boldsymbol{O} \\ \boldsymbol{O} & \boldsymbol{I} & T_s\boldsymbol{I} \\ \boldsymbol{O} & \boldsymbol{O} & 2\boldsymbol{I} \end{bmatrix}, \quad \boldsymbol{A}_{r,x2} = \begin{bmatrix} \boldsymbol{O} & \boldsymbol{O} & \boldsymbol{O} \\ \boldsymbol{O} & \boldsymbol{O} & \boldsymbol{O} \\ \boldsymbol{O} & \boldsymbol{O} & -\boldsymbol{I} \end{bmatrix},$$
$$\boldsymbol{B}_{r,x1} = \begin{bmatrix} \boldsymbol{O} \\ \boldsymbol{O} \\ T_s\hat{\boldsymbol{G}}_{r,x} \end{bmatrix}, \quad \boldsymbol{\xi}_{r,x} = \begin{bmatrix} -T_s\boldsymbol{\omega}_1(k) \\ -T_s\boldsymbol{\omega}_2(k) \\ T_s\tilde{\boldsymbol{\varepsilon}}_{r,x} + T_s\overline{\boldsymbol{\omega}}_3(k) \end{bmatrix}.$$

Define $\boldsymbol{X}_{r,x}(k) = \begin{bmatrix} \boldsymbol{x}_{r,x}(k) & \boldsymbol{x}_{r,x}(k-1) \end{bmatrix}^{\mathrm{T}}$, where $\boldsymbol{x}_{r,x}(k-1)$ denotes the state value of $\boldsymbol{x}_{r,x}(k)$ at the previous time instant. Accordingly, Equation (39) can be expressed as the following first-order discrete-time incremental linear dynamic system.

$$\boldsymbol{X}_{r,x}(k) = \boldsymbol{A}_{r,x}\boldsymbol{X}_{r,x}(k-1) + \boldsymbol{B}_{r,x}\Delta\boldsymbol{u}(k) + \hat{\boldsymbol{\varepsilon}}_{r,x}(k), \tag{40}$$

where $\boldsymbol{A}_{r,x}$, $\boldsymbol{B}_{r,x}$, and $\hat{\boldsymbol{\varepsilon}}_{r,x}$ are respectively given by

$$\boldsymbol{A}_{r,x} = \begin{bmatrix} \boldsymbol{A}_{r,x1} & \boldsymbol{A}_{r,x2} \\ \boldsymbol{I} & \boldsymbol{O} \end{bmatrix}, \quad \boldsymbol{B}_{r,x} = \begin{bmatrix} \boldsymbol{B}_{r,x1} \\ \boldsymbol{O} \end{bmatrix}, \quad \hat{\boldsymbol{\varepsilon}}_{r,x} = \begin{bmatrix} \hat{\boldsymbol{\varepsilon}}_{r,x1} \\ \boldsymbol{O} \end{bmatrix}.$$

Similarly, the discrete-time incremental linear dynamic systems corresponding to Equations (34)–(36) can be derived.

$$\boldsymbol{X}_{r,y}(k) = \boldsymbol{A}_{r,y}\boldsymbol{X}_{r,y}(k-1) + \boldsymbol{B}_{r,y}\Delta\boldsymbol{u}(k) + \hat{\boldsymbol{\varepsilon}}_{r,y}(k), \tag{41}$$
$$\boldsymbol{X}_{r,z}(k) = \boldsymbol{A}_{r,z}\boldsymbol{X}_{r,z}(k-1) + \boldsymbol{B}_{r,z}\Delta\boldsymbol{u}(k) + \hat{\boldsymbol{\varepsilon}}_{r,z}(k), \tag{42}$$
$$\boldsymbol{X}_{V}(k) = \boldsymbol{A}_{V}\boldsymbol{X}_{V}(k-1) + \boldsymbol{B}_{V}\Delta\boldsymbol{u}(k) + \hat{\boldsymbol{\varepsilon}}_{V}(k), \tag{43}$$

where $\boldsymbol{A}_{r,y}$, $\boldsymbol{A}_{r,z}$, $\boldsymbol{A}_{V}$, and $\boldsymbol{B}_{r,y}$, $\boldsymbol{B}_{r,z}$, $\boldsymbol{B}_{V}$ take the same form as $\boldsymbol{A}_{r,x}$ and $\boldsymbol{B}_{r,x}$ in Equation (40).

Similarly,

$$\boldsymbol{X}_{r,y}(k) = \begin{bmatrix} \boldsymbol{x}_{r,y}(k) & \boldsymbol{x}_{r,y}(k-1) \end{bmatrix}^{\mathrm{T}},$$
$$\boldsymbol{X}_{r,z}(k) = \begin{bmatrix} \boldsymbol{x}_{r,z}(k) & \boldsymbol{x}_{r,z}(k-1) \end{bmatrix}^{\mathrm{T}},$$
$$\boldsymbol{X}_{V}(k) = \begin{bmatrix} \boldsymbol{x}_{V}(k) & \boldsymbol{x}_{V}(k-1) \end{bmatrix}^{\mathrm{T}},$$

where

$$\boldsymbol{x}_{r,y}(k) = \begin{bmatrix} \boldsymbol{x}_{r,y1}(k) & \boldsymbol{x}_{r,y2}(k) & \boldsymbol{x}_{r,y3}(k) \end{bmatrix}^{\mathrm{T}},$$
$$\boldsymbol{x}_{r,z}(k) = \begin{bmatrix} \boldsymbol{x}_{r,z1}(k) & \boldsymbol{x}_{r,z2}(k) & \boldsymbol{x}_{r,z3}(k) \end{bmatrix}^{\mathrm{T}},$$
$$\boldsymbol{x}_{V}(k) = \begin{bmatrix} \boldsymbol{x}_{V1}(k) & \boldsymbol{x}_{V2}(k) & \boldsymbol{x}_{V3}(k) \end{bmatrix}^{\mathrm{T}}.$$

The state variable of the approximate discrete-time incremental linear dynamic system is defined as

$$\boldsymbol{X}_{g}(k) = \begin{bmatrix} \boldsymbol{X}_{r,x}(k) & \boldsymbol{X}_{r,y}(k) & \boldsymbol{X}_{r,z}(k) & \boldsymbol{X}_{V}(k) \end{bmatrix}^{\mathrm{T}}. \tag{44}$$

The approximate discrete-time incremental linear dynamic system describing the gliding-phase maneuver model can be formulated as

$$\boldsymbol{X}_{g}(k+1) = \boldsymbol{A}_{g}\boldsymbol{X}_{g}(k) + \boldsymbol{B}_{g}\Delta\boldsymbol{u}(k) + \hat{\boldsymbol{\varepsilon}}_{g}(k), \tag{45}$$

where $\boldsymbol{A}_{g}$, $\boldsymbol{B}_{g}$, and $\hat{\boldsymbol{\varepsilon}}_{g}$ are respectively given by

$$\boldsymbol{A}_g = \begin{bmatrix} \boldsymbol{A}_{r,x} & \boldsymbol{O} & \boldsymbol{O} & \boldsymbol{O} \\ \boldsymbol{O} & \boldsymbol{A}_{r,y} & \boldsymbol{O} & \boldsymbol{O} \\ \boldsymbol{O} & \boldsymbol{O} & \boldsymbol{A}_{r,z} & \boldsymbol{O} \\ \boldsymbol{O} & \boldsymbol{O} & \boldsymbol{O} & \boldsymbol{A}_V \end{bmatrix}, \quad \boldsymbol{B}_g = \begin{bmatrix} \boldsymbol{B}_{r,x} \\ \boldsymbol{B}_{r,y} \\ \boldsymbol{B}_{r,z} \\ \boldsymbol{B}_V \end{bmatrix}, \quad \hat{\boldsymbol{\varepsilon}}_g = \begin{bmatrix} \hat{\boldsymbol{\varepsilon}}_{r,x} \\ \hat{\boldsymbol{\varepsilon}}_{r,y} \\ \hat{\boldsymbol{\varepsilon}}_{r,z} \\ \hat{\boldsymbol{\varepsilon}}_V \end{bmatrix}.$$

Following the common assumption in [24,25], for $\hat{\boldsymbol{\varepsilon}}_g = \boldsymbol{0}$. Then the nominal discrete-time linear system (45) is derived.

$$\boldsymbol{X}_g(k+1) = \boldsymbol{A}_g \boldsymbol{X}_g(k) + \boldsymbol{B}_g \Delta \boldsymbol{u}(k). \tag{46}$$

3.2. IMPC-Based Maneuver Method Under Multiple Constraints

3.2.1. Cost Function Design

Assuming the radar systems predicts the position of the gliding vehicle at time t based on time $t - t_p$, and uses the error between the predicted position at time t and the actual position at time t as the evaluation output $\boldsymbol{Y}(k)$.

$$\boldsymbol{Y}(k) = \begin{bmatrix} r_{\mathrm{H},x}(k) - \hat{r}_{\mathrm{H},x}\left(k_{t|t-t_p}\right) \\ r_{\mathrm{H},y}(k) - \hat{r}_{\mathrm{H},y}\left(k_{t|t-t_p}\right) \\ r_{\mathrm{H},z}(k) - \hat{r}_{\mathrm{H},z}\left(k_{t|t-t_p}\right) \end{bmatrix} = \boldsymbol{C}_g \boldsymbol{X}_g(k) - \boldsymbol{C}_p \hat{\boldsymbol{x}}\left(k_{t|t-t_p}\right), \tag{47}$$

where $\hat{r}_{\mathrm{H},x}\left(k_{t|t-t_p}\right)$, $\hat{r}_{\mathrm{H},y}\left(k_{t|t-t_p}\right)$, $\hat{r}_{\mathrm{H},z}\left(k_{t|t-t_p}\right)$ and $\hat{\boldsymbol{x}}\left(k_{t|t-t_p}\right)$ denote the predicted state value from time $t - t_p$ to t.

$$\boldsymbol{C}_g = \begin{bmatrix} \boldsymbol{C}_{g,x} & \boldsymbol{O}_{1\times 6} & \boldsymbol{O}_{1\times 6} & \boldsymbol{O}_{1\times 6} \\ \boldsymbol{O}_{1\times 6} & \boldsymbol{C}_{g,y} & \boldsymbol{O}_{1\times 6} & \boldsymbol{O}_{1\times 6} \\ \boldsymbol{O}_{1\times 6} & \boldsymbol{O}_{1\times 6} & \boldsymbol{C}_{g,z} & \boldsymbol{O}_{1\times 6} \end{bmatrix},$$

$$\boldsymbol{C}_p = \begin{bmatrix} \boldsymbol{C}_{pI} & \boldsymbol{O}_{1\times 3} & \boldsymbol{O}_{1\times 3} \\ \boldsymbol{O}_{1\times 3} & \boldsymbol{C}_{pI} & \boldsymbol{O}_{1\times 3} \\ \boldsymbol{O}_{1\times 3} & \boldsymbol{O}_{1\times 3} & \boldsymbol{C}_{pI} \end{bmatrix},$$

where $\boldsymbol{C}_{g,x} = \boldsymbol{C}_{g,y} = \boldsymbol{C}_{g,z} = \begin{bmatrix} 1 & 0 & 0 & 0 & 0 & 0 \end{bmatrix}$, $\boldsymbol{C}_{pI} = \begin{bmatrix} 1 & 0 & 0 \end{bmatrix}$.

Definition 3. *The prediction error evaluation output of the radar systems is defined as* $\boldsymbol{Y}(k) = \boldsymbol{C}_g \boldsymbol{X}_g(k) - \boldsymbol{C}_p \hat{\boldsymbol{x}}\left(k_{t|t-t_p}\right)$*, where each component* $\boldsymbol{Y}_i(k) = r_{H,i}(k) - \hat{r}_{H,i}\left(k_{t|t-t_p}\right), i \in \{x, y, z\}$*, represents the difference between the actual position of the gliding vehicle and the position predicted by the radar systems over the prediction interval* t_p*.*

The evaluation output shown in Equation (47) describes the detection effectiveness of the interceptor against the gliding vehicle. The purpose of the maneuver strategy for the gliding vehicle is to maximize the prediction error $\|\boldsymbol{Y}(k)\|$, which is achieved by adjusting the incremental control input $\Delta \boldsymbol{u}$. The control process is subject to the following state and control constraints.

To incorporate nonlinear constraints into the IMPC control framework, these nonlinear constraints are quantitatively transformed. Accordingly, path constraints including heat flux, dynamic pressure, and aerodynamic overload are formulated in incremental form.

$$\begin{bmatrix} \left.\frac{\partial \dot{Q}_{\mathrm{H}}}{\partial V_{\mathrm{H}}}\right|_{V_{\mathrm{H},0}} & -\left.\frac{\partial \dot{Q}_{\mathrm{H}}}{\partial V_{\mathrm{H}}}\right|_{V_{\mathrm{H},0}} \\ \left.\frac{\partial q_{\mathrm{H}}}{\partial V_{\mathrm{H}}}\right|_{V_{\mathrm{H},0}} & -\left.\frac{\partial q_{\mathrm{H}}}{\partial V_{\mathrm{H}}}\right|_{V_{\mathrm{H},0}} \\ \left.\frac{\partial n_{\mathrm{H}}^2}{\partial V_{\mathrm{H}}}\right|_{V_{\mathrm{H},0}} & -\left.\frac{\partial n_{\mathrm{H}}^2}{\partial V_{\mathrm{H}}}\right|_{V_{\mathrm{H},0}} \end{bmatrix} \begin{bmatrix} V_{\mathrm{H}}(k) \\ V_{\mathrm{H}}(k-1) \end{bmatrix} \leq \begin{bmatrix} \dot{Q}_{\mathrm{H,max}} \\ q_{\mathrm{H,max}} \\ n_{\mathrm{H,max}}^2 \end{bmatrix} - \begin{bmatrix} \dot{Q}_{\mathrm{H},0} \\ q_{\mathrm{H},0} \\ n_{\mathrm{H},0}^2 \end{bmatrix}, \tag{48}$$

where

$$\left.\frac{\partial \dot{Q}_{\mathrm{H}}}{\partial V_{\mathrm{H}}}\right|_{V_{\mathrm{H},0}} = k_2 k_{\mathrm{Q}} \rho_{\mathrm{H}}^{k_1} V_{\mathrm{H}}^{k_2-1}\Big|_{V_{\mathrm{H},0}},$$

$$\left.\frac{\partial q_{\mathrm{H}}}{\partial V_{\mathrm{H}}}\right|_{V_{\mathrm{H},0}} = \rho_{\mathrm{H}} V_{\mathrm{H}}|_{V_{\mathrm{H},0}},$$

$$\left.\frac{\partial n_{\mathrm{H}}^2}{\partial V_{\mathrm{H}}}\right|_{V_{\mathrm{H},0}} = \frac{\rho_{\mathrm{H}}^2 S_{\mathrm{H,ref}}^2 \left(C_{\mathrm{L}}^2 + C_{\mathrm{D}}^2\right)}{m_{\mathrm{H}}^2 g_0^2} V_{\mathrm{H}}\Big|_{V_{\mathrm{H},0}}.$$

The constraints in Equation (48) can be converted into state-variable constraint form.

$$\boldsymbol{L}_V \boldsymbol{D}_L \boldsymbol{X}_g(k) \le \boldsymbol{L}_{\max} - \boldsymbol{L}(k), \tag{49}$$

where $\boldsymbol{L}_V$, $\boldsymbol{D}_L$, $\boldsymbol{L}_{\max}$, $\boldsymbol{L}(k)$ are respectively given by

$$\boldsymbol{L}_V = \begin{bmatrix} \left.\frac{\partial \dot{Q}_{\mathrm{H}}}{\partial V_{\mathrm{H}}}\right|_{V_{\mathrm{H},0}} & -\left.\frac{\partial \dot{Q}_{\mathrm{H}}}{\partial V_{\mathrm{H}}}\right|_{V_{\mathrm{H},0}} \\ \left.\frac{\partial q_{\mathrm{H}}}{\partial V_{\mathrm{H}}}\right|_{V_{\mathrm{H},0}} & -\left.\frac{\partial q_{\mathrm{H}}}{\partial V_{\mathrm{H}}}\right|_{V_{\mathrm{H},0}} \\ \left.\frac{\partial n_{\mathrm{H}}^2}{\partial V_{\mathrm{H}}}\right|_{V_{\mathrm{H},0}} & -\left.\frac{\partial n_{\mathrm{H}}^2}{\partial V_{\mathrm{H}}}\right|_{V_{\mathrm{H},0}} \end{bmatrix}, \quad \boldsymbol{L}_{\max} = \begin{bmatrix} \dot{Q}_{\mathrm{H,max}} \\ q_{\mathrm{H,max}} \\ n_{\mathrm{H,max}}^2 \end{bmatrix}, \quad \boldsymbol{L}(k) = \begin{bmatrix} \dot{Q}_{\mathrm{H},0} \\ q_{\mathrm{H},0} \\ n_{\mathrm{H},0}^2 \end{bmatrix},$$

$$\boldsymbol{D}_{\mathrm{L}} = \begin{bmatrix} \boldsymbol{O}_{1\times 6} & \boldsymbol{O}_{1\times 6} & \boldsymbol{O}_{1\times 6} & \boldsymbol{D}_{\mathrm{LI}} \end{bmatrix}, \quad \boldsymbol{D}_{\mathrm{LI}} = \begin{bmatrix} 1 & 0 & 0 & 1 & 0 & 0 \end{bmatrix}.$$

Through the aforementioned constraint quantification process, the process constraints are converted into state constraints, which facilitates the subsequent use of IMPC to solve the optimal control problem under multiple constraints.

Since the control input $\boldsymbol{u}$ is constrained by $|\boldsymbol{u}| \le 1$, the corresponding constraint on the incremental control input is

$$-1 - u_0 \le \Delta \boldsymbol{u} \le 1 - u_0. \tag{50}$$

The aforementioned maneuver problem can be formulated as a constrained optimal control problem (OCP). Specifically, subject to the state constraints in Equation (49) and the control constraints in Equation (50), the optimal incremental control input $\Delta \boldsymbol{u}$ is solved to maximize the prediction errors $\|\boldsymbol{Y}(k)\|$.

3.2.2. IMPC Formulation

Assume the prediction horizon of IMPC is p, and the predicted state sequence over the subsequent p steps can be obtained from Equation (46).

$$\begin{aligned} \boldsymbol{X}_g(k+1|k) &= \boldsymbol{A}_g \boldsymbol{X}_g(k) + \boldsymbol{B}_g \Delta \boldsymbol{u}(k|k), \\ \boldsymbol{X}_g(k+2|k) &= (\boldsymbol{A}_g)^2 \boldsymbol{X}_g(k) + \boldsymbol{A}_g \boldsymbol{B}_g \Delta \boldsymbol{u}(k|k) + \boldsymbol{B}_g \Delta \boldsymbol{u}(k+1|k), \\ &\vdots \\ \boldsymbol{X}_g(k+p+1|k) &= (\boldsymbol{A}_g)^{p+1} \boldsymbol{X}_g(k) + (\boldsymbol{A}_g)^p \boldsymbol{B}_g \Delta \boldsymbol{u}(k|k) + \cdots + \boldsymbol{B}_g \Delta \boldsymbol{u}(k+p|k), \end{aligned} \tag{51}$$

where $k+i|k,\ i = 1, \ldots, p+1$ denotes the prediction from instant k to instant $k+i$.

Define the state vector and control vector as

$$\overline{\boldsymbol{X}}_g(k+1) = \begin{bmatrix} \boldsymbol{X}_g(k+1|k) \\ \boldsymbol{X}_g(k+2|k) \\ \vdots \\ \boldsymbol{X}_g(k+p+1|k) \end{bmatrix}, \tag{52}$$

$$\Delta\overline{\boldsymbol{u}}(k) = \begin{bmatrix} \Delta\boldsymbol{u}(k|k) \\ \Delta\boldsymbol{u}(k+1|k) \\ \vdots \\ \Delta\boldsymbol{u}(k+p|k) \end{bmatrix}. \tag{53}$$

Then the predicted state sequence in Equation (51) can be expressed in the form of a predicted incremental state-space representation.

$$\overline{\boldsymbol{X}}_g(k+1) = \overline{\boldsymbol{A}}_g \boldsymbol{X}_g(k) + \overline{\boldsymbol{B}}_g \Delta\boldsymbol{u}(k), \tag{54}$$

where $\overline{\boldsymbol{A}}_g$ and $\overline{\boldsymbol{B}}_g$ are respectively given by

$$\overline{\boldsymbol{A}}_g = \begin{bmatrix} \boldsymbol{A}_g \\ (\boldsymbol{A}_g)^2 \\ \vdots \\ (\boldsymbol{A}_g)^{p+1} \end{bmatrix}_{(24\times p)\times(24)}, \quad \overline{\boldsymbol{B}}_g = \begin{bmatrix} \boldsymbol{B}_g & \boldsymbol{0}_{14\times 1} & & \\ \boldsymbol{A}_g\boldsymbol{B}_g & \boldsymbol{B}_g & & \\ & & \ddots & \\ (\boldsymbol{A}_g)^p\boldsymbol{B}_g & (\boldsymbol{A}_g)^{p-1}\boldsymbol{B}_g & \cdots & \boldsymbol{B}_g \end{bmatrix}_{(24\times p)\times(p)}.$$

The evaluation output of the predictive incremental linear system in Equation (54) over the prediction horizon of p steps is

$$\overline{\boldsymbol{Y}}(k) = \overline{\boldsymbol{C}}_g \overline{\boldsymbol{X}}_g(k+1) - \overline{\boldsymbol{C}}_p \hat{\boldsymbol{x}}^*(k_{t|t-t_p}), \tag{55}$$

where $\hat{\boldsymbol{x}}^*(k_{t|t-t_p})$ denotes the state sequence estimated over the prediction horizon of p steps, and $\overline{\boldsymbol{C}}_g$ and $\overline{\boldsymbol{C}}_p$ are respectively given by

$$\overline{\boldsymbol{C}}_g = \begin{bmatrix} \boldsymbol{C}_g & \boldsymbol{O}_{3\times 24} & \boldsymbol{O}_{3\times 24} & \\ \boldsymbol{O}_{3\times 24} & \boldsymbol{C}_g & \boldsymbol{O}_{3\times 24} & \\ \boldsymbol{O}_{3\times 24} & \boldsymbol{O}_{3\times 24} & \ddots & \\ & & & \boldsymbol{C}_g \end{bmatrix}_{(3p)\times(24p)}, \quad \overline{\boldsymbol{C}}_p = \begin{bmatrix} \boldsymbol{C}_p & \boldsymbol{O}_{3\times 9} & \boldsymbol{O}_{3\times 9} & \\ \boldsymbol{O}_{3\times 9} & \boldsymbol{C}_p & \boldsymbol{O}_{3\times 9} & \\ \boldsymbol{O}_{3\times 9} & \boldsymbol{O}_{3\times 9} & \ddots & \\ & & & \boldsymbol{C}_p \end{bmatrix}_{(3p)\times(9p)}.$$

Based on the evaluation output $\overline{\boldsymbol{Y}}(k)$, the cost function $J_p\left(\overline{\boldsymbol{X}}_g(k)\right)$ corresponding to the input sequence $\Delta\overline{\boldsymbol{u}}(k)$ at time instant k is defined as

$$\begin{aligned} J_p\left(\overline{\boldsymbol{X}}_g(k), \Delta\overline{\boldsymbol{u}}(k), k\right) &= \sum_{j=1}^{p-1} \sum_{i=x,y,z} \left(r_{\mathrm{H},i}(k+j|k) - \hat{r}_{\mathrm{H},i}\left(k_{t-t_p}+j|k_{t-t_p}\right)\right)^2 \\ &= \overline{\boldsymbol{Y}}^T(k)\overline{\boldsymbol{Y}}(k). \end{aligned} \tag{56}$$

Finally, within the MPC framework, subject to the state constraints (49) and control constraints (50), the incremental predictive control problem of maximizing the cost function $J_p\left(\overline{\boldsymbol{X}}_g(k), \Delta\overline{\boldsymbol{u}}(k), k\right)$ can be formulated as follows:

$$V(\overline{\boldsymbol{X}}_g(k),k) = \max_{\Delta\overline{\boldsymbol{u}}(k)} J_p(\overline{\boldsymbol{X}}_g(k),\Delta\overline{\boldsymbol{u}}(k),k),$$
$$\text{s.t.}\begin{cases}\overline{\boldsymbol{X}}_g(k+1) = \overline{\boldsymbol{A}}_g\boldsymbol{X}_g(k) + \overline{\boldsymbol{B}}_g\Delta\overline{\boldsymbol{u}}(k),\\ \boldsymbol{L}_V\boldsymbol{D}_L\boldsymbol{X}_g(k) \le \boldsymbol{L}_{\max} - \boldsymbol{L}(k),\\ -1-u_0 \le \Delta\boldsymbol{u} \le 1-u_0.\end{cases} \tag{57}$$

The cost function is converted into the minimization formulation suited for MPC algorithm solvers. Therefore, Equation (57) can be rewritten as

$$V(\overline{\boldsymbol{X}}_g(k),k) = \min_{\Delta\overline{\boldsymbol{u}}(k)} \overline{J}_p(\overline{\boldsymbol{X}}_g(k),\Delta\overline{\boldsymbol{u}}(k),k),$$
$$\text{s.t.}\begin{cases}\overline{\boldsymbol{X}}_g(k+1) = \overline{\boldsymbol{A}}_g\boldsymbol{X}_g(k) + \overline{\boldsymbol{B}}_g\Delta\overline{\boldsymbol{u}}(k),\\ \boldsymbol{L}_V\boldsymbol{D}_L\boldsymbol{X}_g(k) \le \boldsymbol{L}_{\max} - \boldsymbol{L}(k),\\ -1-u_0 \le \Delta\boldsymbol{u} \le 1-u_0,\end{cases} \tag{58}$$

where $\overline{J}_p(\overline{\boldsymbol{X}}_g(k),\Delta\overline{\boldsymbol{u}}(k),k) = -J_p(\overline{\boldsymbol{X}}_g(k),\Delta\overline{\boldsymbol{u}}(k),k)$.

Since $\overline{\boldsymbol{B}}_g^\top\overline{\boldsymbol{C}}_g^\top\overline{\boldsymbol{C}}_g\overline{\boldsymbol{B}}_g \succeq \boldsymbol{0}$, J_p in Equation (56) is a convex quadratic function of $\Delta\overline{\boldsymbol{u}}(k)$ and is maximized over a polytope, so that problem (57) is nonconvex. The difficulty therefore lies in the direction of the optimization rather than in the objective, and no approximation of the objective is required at this stage. The state sequence is eliminated by substituting Equation (54) into Equation (55), which leaves J_p as an exact quadratic function of $\Delta\overline{\boldsymbol{u}}(k)$. For this purpose, define the residual at zero increment as

$$\boldsymbol{Y}_0(k) = \overline{\boldsymbol{C}}_g\overline{\boldsymbol{A}}_g\boldsymbol{X}_g(k) - \overline{\boldsymbol{C}}_p\hat{\boldsymbol{x}}^*(k_{t|t-t_p}), \tag{59}$$

which is Equation (55) evaluated at $\Delta\overline{\boldsymbol{u}}(k) = \boldsymbol{0}$. Then $\overline{\boldsymbol{Y}}(k) = \boldsymbol{Y}_0(k) + \overline{\boldsymbol{C}}_g\overline{\boldsymbol{B}}_g\Delta\overline{\boldsymbol{u}}(k)$ and

$$J_p = \|\boldsymbol{Y}_0(k)\|^2 + 2\boldsymbol{Y}_0^\top(k)\overline{\boldsymbol{C}}_g\overline{\boldsymbol{B}}_g\Delta\overline{\boldsymbol{u}}(k) + \Delta\overline{\boldsymbol{u}}^\top(k)\overline{\boldsymbol{B}}_g^\top\overline{\boldsymbol{C}}_g^\top\overline{\boldsymbol{C}}_g\overline{\boldsymbol{B}}_g\Delta\overline{\boldsymbol{u}}(k), \tag{60}$$

whose Hessian with respect to $\Delta\overline{\boldsymbol{u}}(k)$ is $2\overline{\boldsymbol{B}}_g^\top\overline{\boldsymbol{C}}_g^\top\overline{\boldsymbol{C}}_g\overline{\boldsymbol{B}}_g \succeq \boldsymbol{0}$; the negative quadratic form in Equation (60) is therefore concave. The affine function minimized in Equation (58) is the negative of the tangent of Equation (60) at $\Delta\overline{\boldsymbol{u}}(k) = \boldsymbol{0}$,

$$\overline{J}_p^*(\Delta\overline{\boldsymbol{u}}(k)) = -\Big(J_p(\boldsymbol{0}) + \nabla J_p^\top(\boldsymbol{0})\,\Delta\overline{\boldsymbol{u}}(k)\Big), \qquad \nabla J_p(\boldsymbol{0}) = 2\overline{\boldsymbol{B}}_g^\top\overline{\boldsymbol{C}}_g^\top\boldsymbol{Y}_0(k), \tag{61}$$

and is a convex surrogate rather than an equivalent reformulation of Equation (57). The properties of this surrogate that are used in the design are established in Proposition 1.

Based on the affine surrogate in Equation (61), the IMPC problem of minimizing the cost function can be formulated as

$$V(\overline{\boldsymbol{X}}_g(k),k) = \min_{\Delta\overline{\boldsymbol{u}}(k)} \overline{J}_p^*(\overline{\boldsymbol{X}}_g(k),\Delta\overline{\boldsymbol{u}}(k),k),$$
$$\text{s.t.}\begin{cases}\overline{\boldsymbol{X}}_g(k+1) = \overline{\boldsymbol{A}}_g\boldsymbol{X}_g(k) + \overline{\boldsymbol{B}}_g\Delta\overline{\boldsymbol{u}}(k),\\ \boldsymbol{L}_V\boldsymbol{D}_L\boldsymbol{X}_g(k) \le \boldsymbol{L}_{\max} - \boldsymbol{L}(k),\\ -1-u_0 \le \Delta\boldsymbol{u} \le 1-u_0.\end{cases} \tag{62}$$

Proposition 1. *Let $\mathcal{U}(k)$ denote the polytope defined by Equations (49) and (50), and suppose that $\boldsymbol{0} \in \mathcal{U}(k)$. Let $\Delta\overline{\boldsymbol{u}}^*(k)$ be the solution of (62). Then*

1. $J_p\big(\Delta\overline{\boldsymbol{u}}^*(k)\big) \geq J_p(\mathbf{0}) + 2\boldsymbol{Y}_0^\top \overline{\boldsymbol{C}}_g \overline{\boldsymbol{B}}_g \Delta\overline{\boldsymbol{u}}^*(k) \geq J_p(\mathbf{0})$;
2. *for every* $\alpha \in (0,1]$, $J_p\big(\alpha\Delta\overline{\boldsymbol{u}}^*(k)\big)$ *is nondecreasing in* α, *so that the exact line-search maximizer of* J_p *on the segment* $\big[\mathbf{0}, \Delta\overline{\boldsymbol{u}}^*(k)\big]$ *is* $\alpha^* = 1$;
3. *since* $\mathbf{0} \in \mathcal{U}(k)$, *the optimized command is never worse than holding the previous command at the same update, and, being bounded on the reachable set, the realized prediction error remains bounded throughout the maneuver. If the linearization point and the radar prediction were frozen, the recursion would be a monotone ascent on a bounded set and would converge to a point at which* $\Delta_J = 0$ *in Equation* (63).

Proof. Since $\overline{\boldsymbol{B}}_g^\top \overline{\boldsymbol{C}}_g^\top \overline{\boldsymbol{C}}_g \overline{\boldsymbol{B}}_g \succeq \mathbf{0}$, J_p is convex in $\Delta\overline{\boldsymbol{u}}$, and its first-order expansion at the origin is a global underestimator, $J_p(\Delta\overline{\boldsymbol{u}}) \geq J_p(\mathbf{0}) + \nabla J_p^\top(\mathbf{0})\Delta\overline{\boldsymbol{u}}$ for all $\Delta\overline{\boldsymbol{u}}$. The affine function minimized in (62) is the negative of this underestimator. Since $\mathbf{0} \in \mathcal{U}(k)$ and $\Delta\overline{\boldsymbol{u}}^*(k)$ minimizes that affine function over $\mathcal{U}(k)$, it follows that $\nabla J_p^\top(\mathbf{0})\Delta\overline{\boldsymbol{u}}^*(k) \geq 0$, which gives 1. Substituting $\alpha\Delta\overline{\boldsymbol{u}}^*(k)$ into (60) yields $J_p(\alpha\Delta\overline{\boldsymbol{u}}^*) - J_p(\mathbf{0}) = 2\alpha\boldsymbol{Y}_0^\top \overline{\boldsymbol{C}}_g \overline{\boldsymbol{B}}_g \Delta\overline{\boldsymbol{u}}^* + \alpha^2 \|\overline{\boldsymbol{C}}_g \overline{\boldsymbol{B}}_g \Delta\overline{\boldsymbol{u}}^*\|^2$, whose derivative with respect to α is $2\boldsymbol{Y}_0^\top \overline{\boldsymbol{C}}_g \overline{\boldsymbol{B}}_g \Delta\overline{\boldsymbol{u}}^* + 2\alpha\|\overline{\boldsymbol{C}}_g \overline{\boldsymbol{B}}_g \Delta\overline{\boldsymbol{u}}^*\|^2 \geq 0$, which gives (2). Statement (3) follows by applying (1) at successive control updates and by boundedness of J_p on the reachable set. □

Proposition 1 settles the monotonicity question. The solution of the affine program is not merely a stationary point of a local model: it is a certified ascent step of the original index, and the realized increase is at least the increase predicted by the affine model, $2\boldsymbol{Y}_0^\top \overline{\boldsymbol{C}}_g \overline{\boldsymbol{B}}_g \Delta\overline{\boldsymbol{u}}^*$, augmented by the nonnegative second-order term $\|\overline{\boldsymbol{C}}_g \overline{\boldsymbol{B}}_g \Delta\overline{\boldsymbol{u}}^*\|^2$. Statement (ii) also shows that no line search is needed for monotonicity: the full step is the exact line-search solution on the segment, and a backtracking test on the nonlinear prediction is applied to the candidate step, in which the step is halved up to three times unless the index does not decrease; the previous command is held if no admissible step is found.

Two qualifications follow. First, $\Delta\overline{\boldsymbol{u}}^*(k)$ is not the global maximizer of (57). Since J_p is convex and $\mathcal{U}(k)$ is a polytope, every global maximizer is a vertex of $\mathcal{U}(k)$, and the solution of (62) is also a vertex; the two may differ, and the difference is quantified against the nonlinear-optimization benchmark in Figure 10a. Second, because J_p is convex, no interior stationary point exists and the KKT-based convergence statements commonly used for nonlinear programming do not apply. The stationarity measure adopted here is instead the Frank–Wolfe gap

$$\Delta_J(k) = \max_{\Delta\overline{\boldsymbol{u}} \in \mathcal{U}(k)} \nabla J_p^\top(\mathbf{0})\, \Delta\overline{\boldsymbol{u}} = 2\boldsymbol{Y}_0^\top(k) \overline{\boldsymbol{C}}_g \overline{\boldsymbol{B}}_g \Delta\overline{\boldsymbol{u}}^*(k), \tag{63}$$

which is available at no extra computational cost, since it is the optimal value of the affine program (62). The condition $\Delta_J(k) = 0$ is equivalent to $\nabla J_p^\top(\mathbf{0})(\boldsymbol{v} - \mathbf{0}) \leq 0$ for all $\boldsymbol{v} \in \mathcal{U}(k)$, i.e., to the absence of a feasible first-order ascent direction at the current prediction sequence.

The optimal state and control sequences are obtained by solving the performance-index-maximizing IMPC problem.

$$\overline{\boldsymbol{X}}_g^*(k+1) = \begin{bmatrix} \boldsymbol{X}_g^*(k+1|k) \\ \boldsymbol{X}_g^*(k+2|k) \\ \vdots \\ \boldsymbol{X}_g^*(k+p+1|k) \end{bmatrix}, \quad \Delta\overline{\boldsymbol{u}}^*(k) = \begin{bmatrix} \Delta\boldsymbol{u}^*(k|k) \\ \Delta\boldsymbol{u}^*(k+1|k) \\ \vdots \\ \Delta\boldsymbol{u}^*(k+p|k) \end{bmatrix}.$$

The first element $\Delta\boldsymbol{u}^*(k|k)$ of the optimal control sequence $\Delta\overline{\boldsymbol{u}}^*(k)$ solved from the above problem corresponds to the optimal incremental control input of the aircraft at the current time instant.

The optimization is not solved at every integration step. A new command is computed every $T_c = 5$ s, and the previous command is held in between. This is consistent with the bang-bang character of the solution, which stays at a bound over several seconds. Accordingly, one convex program is solved per control update, and none at the 249 integration steps in between, at which only the prediction is propagated and the command is held.

Remark 9. *The scheme defined by Equation (62) is a single-iteration sequential convex programming method, equivalent to a conditional-gradient step on the concave form of the index, and the admissible set of Equations (49) and (50) serves as its trust region. The radius of this region is fixed by the actuator envelope rather than by a tuning parameter:* $|\Delta u_i| \leq 1$ *is equivalent to* $|\dot{\sigma}_H| \leq 20^\circ \cdot s^{-1}$*, so that the bank angle can change by at most* 100° *between two successive linearizations at* $T_c = 5$ *s, while the limit* $|\sigma_H| \leq 89^\circ$ *and the incremental process constraints bound the remainder of the motion. Because the index is convex in* $\Delta\overline{\boldsymbol{u}}$*, the affine model is a global underestimator rather than a local approximation, and Proposition 1 guarantees that each step increases the original index. The problem remains nonconvex and is solved over a finite horizon without terminal cost or terminal constraints; the command obtained is therefore a local maximizer of Equation (57), and no recursive-feasibility or closed-loop stability property is claimed.*

In summary, this section has developed a complete IMPC-based maneuver design framework. The nonlinear guidance dynamics were first converted into a weakly model-dependent incremental linear system with a bounded residual. A prediction-error cost function and incrementalized process constraints were then introduced, and the non-convex maneuver optimization problem was approximated by a tractable convex program whose solution is a certified ascent step of the prediction-error index. The resulting algorithm provides bank-angle commands that amplify radar prediction errors under multiple flight constraints, setting the stage for the simulation validation in Section 4.

4. Simulation Results

Numerical simulations are performed to reproduce the complete detection and tracking loop of the radar systems for gliding vehicles, so as to verify the effectiveness of the proposed maneuver method. Firstly, the effectiveness of the IMPC-based method in maximizing the position-prediction errors of the radar systems for a gliding vehicle is verified. Secondly, a comparative analysis is performed on the system performance of the proposed maneuver method under different operating conditions and the approximation capability of the weak model-dependent incremental system to the original nonlinear system. Finally, the simulation results are discussed and analyzed in detail to further demonstrate the rationality and superiority of the proposed method.

4.1. Validation of Effectiveness

In the proposed IMPC method that maximizes the interceptor's prediction errors, when the constant matrices $\hat{\boldsymbol{G}}_{r,x}$, $\hat{\boldsymbol{G}}_{r,y}$, $\hat{\boldsymbol{G}}_{r,z}$, and $\hat{\boldsymbol{G}}_V$ satisfy

$$\left\| \hat{\boldsymbol{G}}_i^{-1} \boldsymbol{g}_i(\boldsymbol{x}_i) - \boldsymbol{I} \right\| \leq c_b < 1, \tag{64}$$

where $i \in \{\{r,x\},\{r,y\},\{r,z\},V\}$.

The incremental error of the system is bounded. Through incremental linearization, the original nonlinear system is transformed into an incremental linear dynamic system, which has a low degree of dependence on specific models. In the simulation, $\hat{G}_{r,x}$, $\hat{G}_{r,y}$, $\hat{G}_{r,z}$ and $\hat{G}_V$ in the subsystem are set as

$$\hat{G}_{r,x} = 3, \quad \hat{G}_{r,y} = 3, \quad \hat{G}_{r,z} = 0.5, \quad \hat{G}_V = -0.005.$$

The incremental control input $\Delta \boldsymbol{u}$ is obtained by solving the constrained optimal control problem formulated in Equation (62). In the practical simulation validation, this problem is solved using the CPLEX toolbox in MATLAB R2022b. The constant matrices $\hat{G}_{r,x}$, $\hat{G}_{r,y}$, $\hat{G}_{r,z}$, and $\hat{G}_V$ can be further refined at each iteration through the following adjustment scheme:

1. For each element of matrices $\hat{G}_{r,x}$, $\hat{G}_{r,y}$, $\hat{G}_{r,z}$, and $\hat{G}_V$, a sufficiently large positive value or a sufficiently small negative value is selected initially. The choice of sign depends on the sign of the eigenvalues of the incremental linear dynamic system Equation (45): a negative value is chosen if the eigenvalue is negative, and a positive value is chosen otherwise.
2. If the value is positive, it is decreased gradually; if it is negative, it is increased gradually. This continues until the incremental linear error converges to a sufficiently small neighborhood.

Through the above steps, the IMPC maneuver method based on the weakly model-dependent incremental linear dynamic system can be implemented successfully.

The simulation parameter settings are as follows (see Table 1):

Table 1. Simulation parameters for gliding vehicle maneuver.

Parameter	Symbol	Value
Vehicle mass	$m_{\mathrm{H}}(\mathrm{kg})$	907.2
Reference area	$S_{\mathrm{H,ref}}(\mathrm{m}^2)$	0.4839
Atmospheric scale height	$\beta(\mathrm{m}^{-1})$	$1/7110$
Initial altitude	$h(\mathrm{m})$	52310
Max angle-of-attack rate	$\dot{\alpha}(\mathrm{rad}\cdot\mathrm{s}^{-1})$	$5\pi/180$
Flight path angle	$\theta_{\mathrm{H}}(\mathrm{rad})$	$0.2\pi/180$
Heading angle	$\psi_{\mathrm{H}}(\mathrm{rad})$	$80\pi/180$
Bank angle	$\sigma_{\mathrm{H}}(\mathrm{rad})$	$0.1\pi/180$
Max heat flux	$\dot{Q}_{\mathrm{H,max}}(\mathrm{kW}\cdot\mathrm{m}^{-2})$	1500
Max dynamic pressure	$q_{\mathrm{H,max}}(\mathrm{kPa})$	100
Max aerodynamic overload	$n_{H,\mathrm{max}}$	3
Simulation step size	$T_{\mathrm{s}}(\mathrm{s})$	0.02
Control update interval	$T_{\mathrm{c}}(\mathrm{s})$	5
Prediction horizon	p	100
Initial position	$(r_{\mathrm{H},x}, r_{\mathrm{H},y}, r_{\mathrm{H},z})(\mathrm{km})$	$(4.76, 52.31, 27.30)$
Initial velocity	$(V_{\mathrm{H},x}, V_{\mathrm{H},y}, V_{\mathrm{H},z})(\mathrm{m}\cdot\mathrm{s}^{-1})$	$(1157, -2.01, -6775)$
Initial acceleration	$(a_{\mathrm{H},x}, a_{\mathrm{H},y}, a_{\mathrm{H},z})(\mathrm{m}\cdot\mathrm{s}^{-2})$	$(-0.52, -8.44, -1.65)$
Acceleration coefficient	$\alpha_i,\ i = x, y, z(\mathrm{s}^{-1})$	0.01
Max lift-to-drag ratio	$(Y_{\mathrm{H}}/X_{\mathrm{H}})_{\mathrm{max}}$	3.5
Max bank angle rate	$\dot{\sigma}_{\mathrm{H,max}}(\mathrm{rad}\cdot\mathrm{s}^{-1})$	$20\pi/180$
Process noise covariance	$\boldsymbol{Q}_k$	$0.01\cdot\mathrm{diag}(1,0,0,1,0,0,1,0,0)^2$
Measurement noise covariance	$\boldsymbol{R}_{k+1}$	$\mathrm{diag}(1000, 2.5\times10^{-4}, 2.5\times10^{-4})^2$
Error covariance matrix	$\boldsymbol{P}_{k\|k}$	$\boldsymbol{I}_{9\times9}$
Heat flux parameter	$(k_{\mathrm{Q}}, k_1, k_2)$	$(3.5\times10^{-5}, 0.5, 3.15)$

The maneuver efficiency of the IMPC-based maneuver strategy in maximizing the prediction errors is verified through comparative simulations against the constant-control-input maneuver approach. For simplicity, the scheme using a fixed control input is denoted as the constant-control method, while the proposed evasive scheme is referred to as the IMPC-based maneuver method. In the IMPC-based maneuver method, the gliding vehicle executes the evasive maneuver designed in this paper, with maneuver initiation at 6 s.

A direct comparison of prediction-error behaviors under different target maneuver patterns is provided in Figures 2 and 3. Figure 2 illustrates the overall position prediction

errors for constant-control and IMPC maneuver flight cases, and Figure 3 further depicts their decomposed three-axis (X, Y, Z) positional error components. As shown in the plotted curves, both aggregate errors and individual axial components become markedly larger for the maneuvering scenario relative to the constant-control counterpart. The radar tracking framework adopts an EKF embedded with the Singer acceleration model for trajectory estimation, and no extra error compensation is available on the radar side. Under such settings, the maneuvering target yields its maximum prediction error of roughly 1200 m near the simulation instant of 32 s.

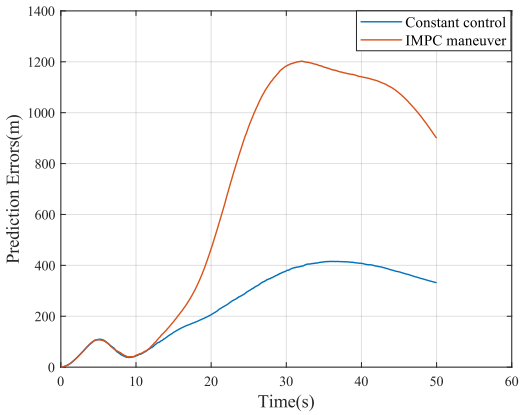

Figure 2. Position prediction errors: IMPC maneuver and constant-control methods.

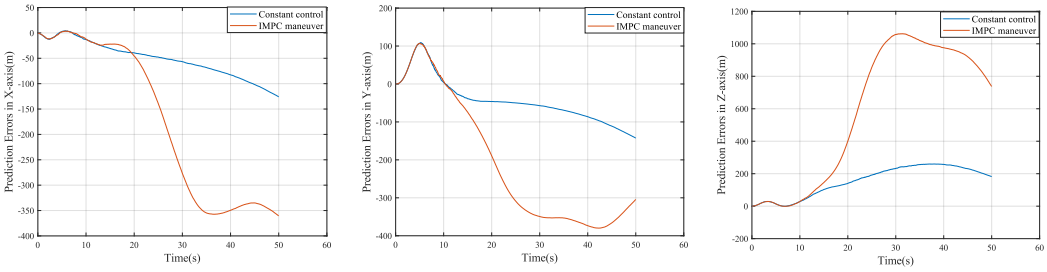

(**a**) (**b**) (**c**)

Figure 3. Position prediction errors on the X, Y, Z axes: IMPC maneuver and constant-control methods. (**a**) Position prediction errors on the X-axis. (**b**) Position prediction errors on the Y-axis. (**c**) Position prediction errors on the Z-axis.

Based on the above error quantitative analysis, Figure 4 illustrates the three-dimensional true trajectory and the corresponding predicted trajectory generated by the radar systems for both maneuvering and non-maneuvering methods. Figure 4a depicts the true and predicted trajectories under the maneuvering method, whereas Figure 4b presents those under the non-maneuvering method. It can be observed more intuitively that the radar systems exhibit a substantially larger tracking and prediction deviation for the vehicle trajectory in the maneuvering method, in contrast to the minor deviation in the non-maneuvering method. Since the separation between the two curves in Figure 4 is the same quantity plotted in Figure 2, its magnitude can be stated explicitly: the maximum deviation, 1200 m at 32 s in the IMPC maneuver case against 410 m at 33 s in the constant control case, corresponds to a maximum separation of about 1.2 km between the true and the predicted trajectories in Figure 4a, whereas the corresponding separation in Figure 4b is about 0.4 km. The advantage is not confined to the peak, since at the end of the tracking window (t = 50 s) the deviations are 900 m and 330 m, respectively, so that the amplification factor, 2.9 at the peak and 2.7 at the final instant, is retained rather than decaying with time.

This result demonstrates that the proposed maneuver strategy effectively amplifies the position-prediction errors of the radar systems.

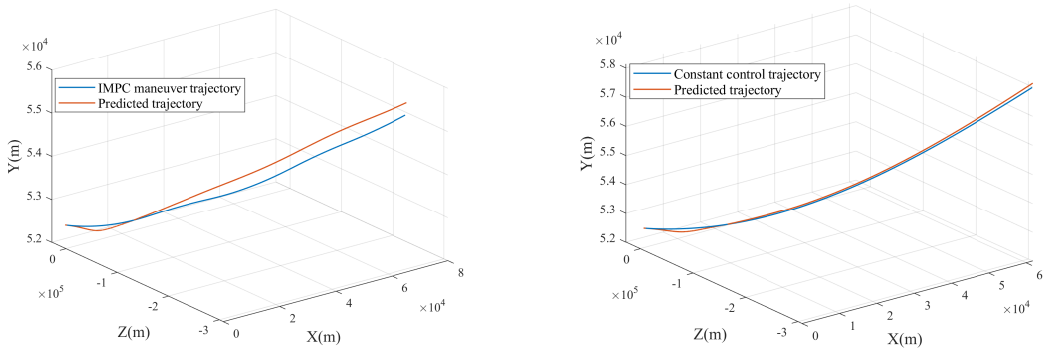

(**a**) (**b**)

Figure 4. Detection system predicted trajectories: IMPC maneuver and constant-control gliding vehicle. (**a**) IMPC maneuver trajectory and its predicted trajectory. (**b**) Constant-control trajectory and its predicted trajectory.

The mechanism of prediction-error amplification enabled by the presented strategy is revealed in Figure 5, which compares the control inputs and bank angles between the IMPC maneuver and constant-control scenarios. Figure 5a plots the time histories of control commands for the two cases. The control update law is formulated as $\boldsymbol{u}^*(k+1) = \boldsymbol{u}(k) + \Delta\boldsymbol{u}^*(k)$, where $\Delta\boldsymbol{u}^*(k)$ denotes the optimal incremental control solved online by the error-maximizing IMPC framework. As illustrated in Figure 5a, the control input remains fixed at $u = 0.001$ for the constant-control case. By contrast, the IMPC-generated control follows a bang–bang saturated profile at its upper/lower bounds to deliberately enlarge trajectory prediction errors. Figure 5b depicts the resultant bank-angle responses driven by respective control laws, whose fluctuation tendency closely coincides with the bang–bang saturation characteristic of the optimized control signal.

Figure 6 shows the computation time of the control update in the IMPC-based maneuver method. The solver is called every 5 s rather than at every integration step, so the 50 s run contains 9 calls. Seven calls finish below 0.15 s. The two longest, near 10 s and 30 s, coincide with the bank-angle reversals, where the active constraint set changes. Over all calls the mean is 0.18665 s and the maximum is 0.58552 s. The maximum is 11.7% of the update interval and 29% of the shortest reversal interval used in Table 2, so a command is always available before the next one is due.

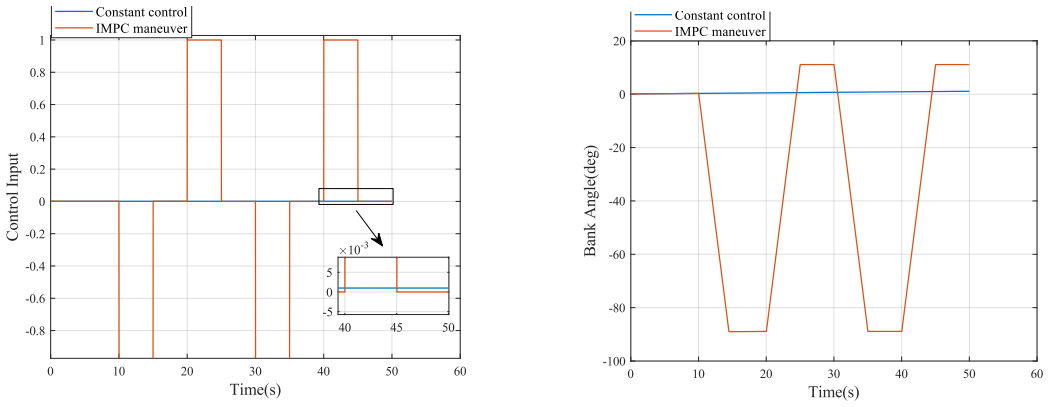

(**a**) Control input. (**b**) Bank angle.

Figure 5. Control input and bank angle: IMPC maneuver and constant-control methods.

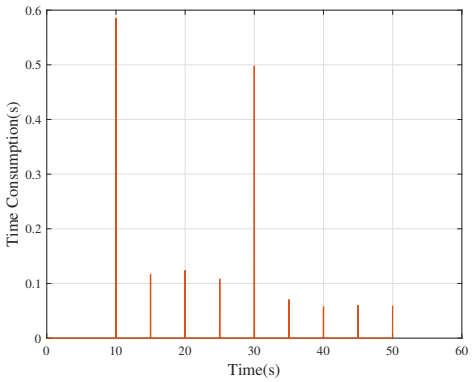

Figure 6. Computation time for control input solution in IMPC maneuver method.

Figure 7 shows the process constraint variations of the gliding vehicle during the detection and tracking process of the maneuvering countermeasure against radar systems, confirming that the proposed maneuver motion satisfies practical flight limits. It can be seen from the figure that the changes in the vehicle's heat flux, dynamic pressure and aerodynamic overload do not exceed the maximum constraint values in this paper, which are 1500 kW $\cdot$ m^{-2}, 100 kPa and 3, respectively.

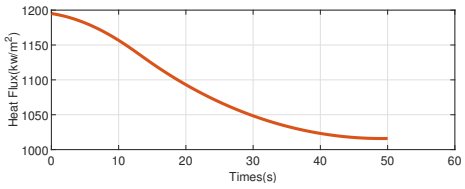

(**a**) Variation of heat flux.

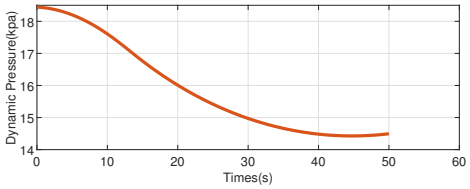

(**b**) Variation of dynamic pressure.

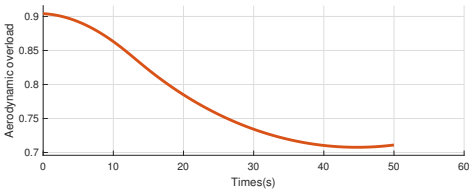

(**c**) Variation of aerodynamic overload.

Figure 7. Process constraint variations of the gliding vehicle.

Table 2. Bank angle reversal times and maximum prediction errors under different maneuvering time intervals.

Maneuvering Time Interval(s)	Bank Angle Reversal Times	Maximum Prediction Errors(m)
2	11	702.1
4	6	858.3
6	4	1365
8	3	1274
10	2	1851
12	2	1939

4.2. Comparative Test

Comparative simulations are performed to investigate the effects of maneuver time intervals on radar prediction errors. The simulation results are shown in Figures 8 and 9 and Table 2. Figure 8 shows the comparison of prediction errors at different maneuver time intervals, and Figure 9 presents the variation of bank angle at these different maneuver time intervals. Their results are summarized in Table 2.

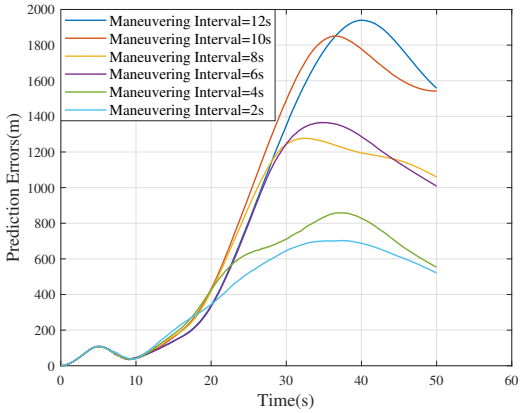

Figure 8. Prediction errors at different maneuvering time intervals.

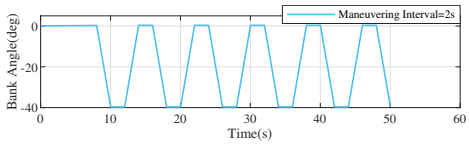

(**a**) The maneuvering time interval is 2 s.

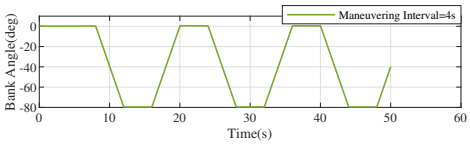

(**b**) The maneuvering time interval is 4 s.

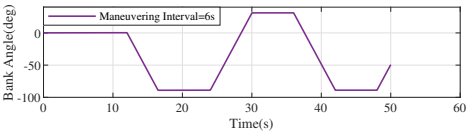

(**c**) The maneuvering time interval is 6 s.

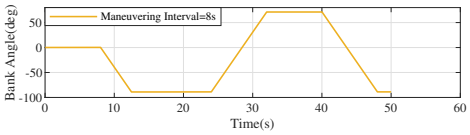

(**d**) The maneuvering time interval is 8 s.

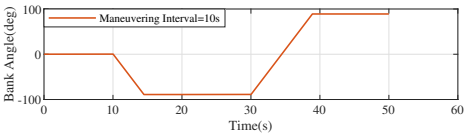

(**e**) The maneuvering time interval is 10 s.

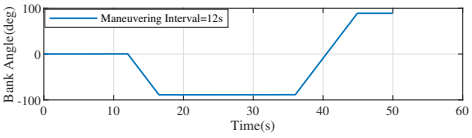

(**f**) The maneuvering time interval is 12 s.

Figure 9. Variations of the bank angle at different maneuvering time intervals.

The bank-angle histories in Figure 9 show two distinct shapes. At a 2 s interval the bank angle follows a trapezoidal profile, in which rate-saturated ramps at the maximum bank rate of 20 deg/s alternate with dwell plateaus. The peak excursion is approximately -40 deg, well below the maximum bank angle of 89 deg, and the plateaus correspond to intervals in which the incremental command is held near zero. At intervals of 6 s and above the bank angle reaches this limit and remains there, so the corresponding profiles are flat-topped. The prediction error is governed by the alternation period rather than by the occurrence of saturation. The lateral displacement is obtained by double integration of the lateral acceleration, so its magnitude is set by the time over which the lateral velocity is permitted to accumulate in one direction. At this interval the bank angle changes sign every 2 s, and the lateral velocity accumulated within one half-cycle is largely removed during the next, so the net lateral deviation remains small. Extending the interval lengthens the alternation period, a larger fraction of the lateral velocity survives each sign change, and the deviation grows accordingly. For the 10 s and 12 s cases the bank angle is held at one of its limits for more than 10 s and changes sign only once within the maneuver window, so the prediction error attains its largest values, 1851 m and 1939 m. This dependence is not monotonic. The 8 s case gives 1274 m, below the 1365 m obtained at 6 s. The difference is 91 m, about 7% of the 6 s value. Since the reversal instants are integer multiples of the interval, they fall at different positions relative to the prediction window, and a phase

effect of this size is sufficient to account for the discrepancy. The overall trend is set by the alternation period; the 8 s case departs from it.

Figure 10 compares the prediction errors and computational time consumption between the developed convex optimization-based IMPC scheme and the conventional nonlinear optimization method. Figure 10a presents the quantitative comparison of prediction errors for the two approaches. The results indicate that the convex optimization-based IMPC method produces slightly smaller prediction errors than the nonlinear optimization method, indicating a minor performance loss in terms of peak error magnification. This difference stems from the inherent linearization approximation: the nonlinear system is converted into an incremental linear dynamic system via quantitative linearization, and unavoidable approximation errors are introduced during this process, even though the resultant incremental linearization error remains bounded. In contrast, nonlinear optimization possesses higher solution accuracy owing to its direct solution of the original nonlinear model. Such approximation deviations can be further mitigated by increasing the system sampling frequency. Although nonlinear optimization outperforms the proposed IMPC scheme in maximizing trajectory prediction errors, it suffers from significantly higher computational consumption in control input solving. The detailed time consumption comparison is illustrated in Figure 10b.

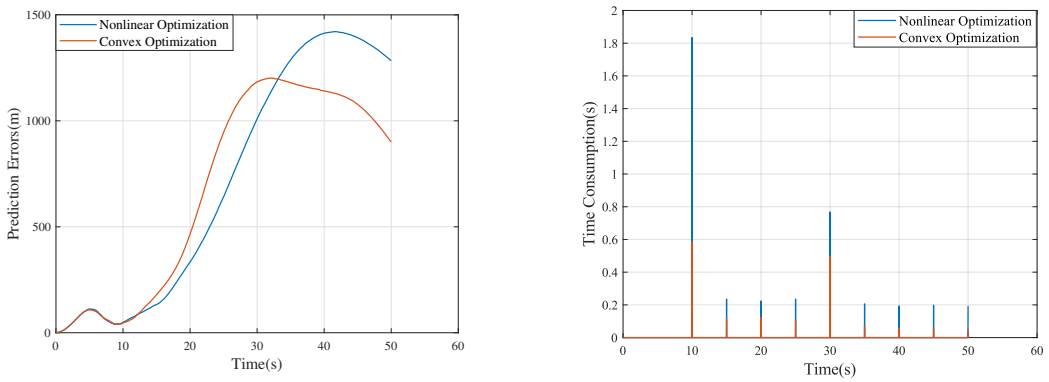

(**a**) (**b**)

Figure 10. Comparison of prediction errors and solution time consumption under nonlinear and convex optimization. (**a**) Comparison of prediction errors. (**b**) Comparisons of solution time consumption.

Table 3 lists the average and maximum computation times for solving control input using nonlinear optimization and convex optimization, respectively. It can be observed from Table 3 that the average and maximum computation times of the nonlinear optimization method are 0.45444 s and 1.83550 s, whereas those of the convex optimization method are 0.18665 s and 0.58552 s. Therefore, the convex optimization approach outperforms the nonlinear optimization method in terms of computation efficiency for control input solutions.

Table 3. Mean and maximum computation time of control input.

Method	Mean Time (s)	Max Time (s)
Nonlinear Opt.	0.45444	1.83550
Convex Opt.	0.18665	0.58552

To verify the rationality and approximation accuracy of the established incremental modeling approach, Figure 11 compares the prediction errors obtained from the nonlinear system and the approximate discrete incremental system. It can be observed that the

prediction errors curves of the two systems match closely, which validates that the nonlinear system can be well approximated by the proposed approximate discrete incremental system. The slight deviation between them arises from the incremental linearization error. With a sufficiently high sampling frequency, the approximate discrete incremental system can achieve high-fidelity approximation to the original nonlinear system. Figure 11 also gives the quantitative comparison. The prediction errors of the incremental approximation follow those of the nonlinear system throughout the maneuver, and the difference between the two curves stays below 25 m, about 2% of the 1200 m peak. The bound in Equation (29) is therefore small in the closed loop as well as in the single step.

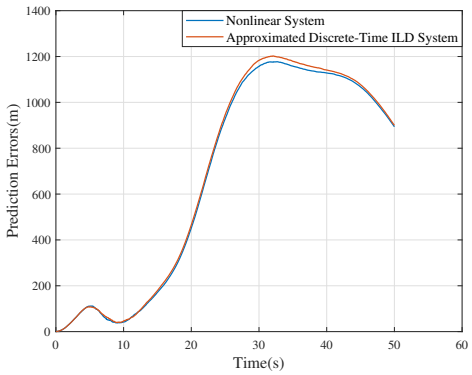

Figure 11. Comparison of prediction errors under nonlinear and approximate discrete incremental systems.

4.3. Discussion and Analysis

The above simulation results verify the effectiveness of the proposed maneuver method, which amplifies the position-prediction errors imposed on the radar systems against a gliding vehicle. As observed from the simulations, the control input generated by the prediction error maximizing IMPC scheme exhibits a typical bang-bang maneuver profile. Compared with the nonlinear programming solution, the proposed IMPC approach achieves slightly inferior performance in terms of peak position-prediction errors; nevertheless, the mean computation time per control update falls from 0.45444 s to 0.18665 s and the maximum from 1.83550 s to 0.58552 s, both within the 5 s update interval. Further comparative results show that the closed-loop prediction errors obtained with the incremental model track those of the nonlinear system to within 25 m throughout the maneuver, about 2% of the peak error in the considered case.

5. Conclusions

The three problems raised at the end of Section 2 were addressed through the proposed incremental modeling, the prediction-error index and the convex surrogate of the online optimization, respectively. This paper investigated the maneuvering problem of gliding vehicles during the detection and tracking phase of radar systems. A maneuver strategy that aimed to maximize the prediction errors during the detection and tracking phase of radar systems was proposed, and a corresponding maneuver approach for a gliding vehicle was developed based on the IMPC framework. With the TSS principle applied, the nonlinear guidance and control system was transformed into an incrementally linear dynamic system with a cascade control structure, which was updated using high-frequency sampled state measurements collected by onboard sensors. A cost function based on prediction errors was formulated to quantify the detection and tracking capability of radar systems, and nonlinear process constraints were addressed through incremental model reformulation. Accordingly, the maneuver optimization problem for the detection and tracking phase was converted into a constrained optimal control problem. Comparative

simulations under the considered scenario were carried out to examine the effectiveness of the developed method. Numerical results show that the IMPC method enables quantitative analysis of the maneuver effectiveness. Compared with the constant-control method, the control input obtained from the IMPC method amplifies the radar prediction error and enhances the survivability of the gliding vehicle, while the computation time per control update is substantially shortened and the dependence on an accurate model is lower. The proposed IMPC method is applicable to the design of active survivability strategies for flight vehicles, and remains applicable in scenarios where an accurate model is difficult to obtain, so that the dependence on the nominal model is reduced. The present validation is restricted to a single deterministic scenario, in which the radar side employs a Singer-model-based EKF and the vehicle model is not perturbed. Quantification of the robustness margin under parameter perturbations and unmodeled dynamics, and the extension to other radar tracking models, are left for future work.

Author Contributions: Conceptualization, H.S. and Z.L.; methodology, H.S. and Z.L.; software, Z.L. and X.W.; validation, Z.L.; formal analysis, X.W. and S.W.; investigation, Y.W.; resources, Y.G.; data curation, Y.W.; writing—original draft preparation, Z.L.; writing—review and editing, X.W. and S.W.; visualization, Z.L.; supervision, Y.G.; project administration, H.S.; funding acquisition, Y.G. All authors have read and agreed to the published version of the manuscript.

Funding: This work was supported by the National Natural Science Foundation of China (Grant No. 62473375).

Data Availability Statement: The data presented in this study are available upon request from the corresponding author.

Conflicts of Interest: The authors declare no conflicts of interest.

Abbreviations

The following abbreviations are used in this manuscript:

IMPC	Incremental model predictive control
LOS	Longitudinal line-of-sight
TSS	Time-scale separation

References

1. Khawaja, W.; Ezuma, M.; Semkin, V.; Erden, F.; Ozdemir, O.; Guvenc, I. A survey on detection, classification, and tracking of AAVs using radar and communications systems. *IEEE Commun. Surv. Tutor.* **2026**, *28*, 3272–3310. https://doi.org/10.1109/COMST.2025.3554613.
2. Chen, J.Q.; Sun, R.S.; Lu, Y. Cooperative game penetration guidance for multiple hypersonic vehicles under safety critical framework. *Chin. J. Aeronaut.* **2024**, *37*, 247–255. https://doi.org/10.1016/j.cja.2023.08.023.
3. Ding, Y.B.; Yue, X.K.; Chen, G.S.; Si, J.S. Review of control and guidance technology on hypersonic vehicle. *Chin. J. Aeronaut.* **2022**, *35*, 1–18. https://doi.org/10.1016/j.cja.2021.10.037.
4. Li, Z.H.; Yang, X.J.; Sun, X.D.; Liu, G.; Hu, C. Improved artificial potential field based lateral entry guidance for waypoints passage and no-fly zones avoidance. *Aerosp. Sci. Technol.* **2019**, *86*, 119–131. https://doi.org/10.1016/j.ast.2019.01.015.
5. Shen, Z.P.; Yu, J.L.; Dong, X.W.; Hua, Y.C.; Ren, Z. Penetration trajectory optimization for the hypersonic gliding vehicle encountering two interceptors. *Aerosp. Sci. Technol.* **2022**, *121*, 107363. https://doi.org/10.1016/j.ast.2022.107363.
6. Huang, A.; Yu, J.L.; Liu, Y.M.; Hua, Y.C.; Dong, X.W.; Ren, Z. Multitask-constrained reentry trajectory planning for hypersonic gliding vehicle. *Aerosp. Sci. Technol.* **2024**, *155*, 109636. https://doi.org/10.1016/j.ast.2024.109636.
7. Yu, W.B.; Chen, W.C.; Jiang, Z.G.; Zhang, W.Q.; Zhao, P.L. Analytical entry guidance for coordinated flight with multiple no-fly-zone constraints. *Aerosp. Sci. Technol.* **2019**, *84*, 273–290. https://doi.org/10.1016/j.ast.2018.10.013.
8. Hu, Y.D.; Gao, C.S.; Li, J.L.; Jing, W.X.; Chen, W.X. A novel adaptive lateral reentry guidance algorithm with complex distributed no-fly zones constraints. *Chin. J. Aeronaut.* **2022**, *35*, 128–143. https://doi.org/10.1016/j.cja.2021.06.016.
9. Liang, Z.X.; Liu, S.Y.; Li, Q.D.; Ren, Z. Lateral entry guidance with no-fly zone constraint. *Aerosp. Sci. Technol.* **2017**, *60*, 39–47. https://doi.org/10.1016/j.ast.2016.10.025.

10. Zhang, D.; Liu, L.; Wang, Y.J. On-line reentry guidance algorithm with both path and no-fly zone constraints. *Acta Astronaut.* **2015**, *117*, 243–253. https://doi.org/10.1016/j.actaastro.2015.08.006.
11. Liang, Z.X.; Ren, Z. Tentacle-based guidance for entry flight with no-fly zone constraint. *J. Guid. Control Dyn.* **2018**, *41*, 996–1005. https://doi.org/10.2514/1.G003157.
12. Wang, X.T.; Yang, M.; Wang, S.Y.; Hou, M.Z.; Chao, T. Linear-quadratic and norm-bounded combined differential game guidance scheme with obstacle avoidance for attacking defended aircraft in three-player engagement. *Def. Technol.* **2024**, *42*, 136–155. https://doi.org/10.1016/j.dt.2024.06.018.
13. Li, X.; Cai, G.B.; Xu, H.; Zhu, J.W.; Mu, C.X. Longitudinal optimal analytical midcourse guidance for cruise-glide integrated hypersonic vehicles. *Def. Technol.* **2025**, *50*, 288–303. https://doi.org/10.1016/j.dt.2025.04.020.
14. Yu, X.J.; Luo, S.B.; Liu, H.Q. Integrated design of multi-constrained snake maneuver surge guidance control for hypersonic vehicles in the dive segment. *Aerospace* **2023**, *10*, 765. https://doi.org/10.3390/aerospace10090765.
15. Zhu, J.; He, R.; Tang, G.; Bao, W.M. Pendulum maneuvering strategy for hypersonic glide vehicles. *Aerosp. Sci. Technol.* **2018**, *78*, 62–70. https://doi.org/10.1016/j.ast.2018.03.038.
16. Guo, Y.; Yao, Y.; Wang, S.C.; Yang, B.Q.; He, F.H.; Zhang, P. Maneuver control strategies to maximize prediction errors in ballistic middle phase. *J. Guid. Control Dyn.* **2013**, *36*, 1225–1234. https://doi.org/10.2514/1.56818.
17. Guo, Y.; Yao, Y.; Wang, S.C.; Yang, B.Q.; Zhang, P. Maneuver strategy of evader considering detection system. In Proceedings of the AIAA Guidance, Navigation, and Control Conference, Portland, OR, USA, 8–11 August 2011. https://doi.org/10.2514/6.2011-6713.
18. Mayne, D.Q.; Rawlings, J.B.; Rao, C.V.; Scokaert, P.O.M. Constrained model predictive control: Stability and optimality. *Automatica* **2000**, *36*, 789–814. https://doi.org/10.1016/S0005-1098(99)00214-9.
19. Eklund, J.M.; Sprinkle, J.; Sastry, S.S. Switched and symmetric pursuit/evasion games using online model predictive control with application to autonomous aircraft. *IEEE Trans. Control Syst. Technol.* **2012**, *20*, 604–620. https://doi.org/10.1109/TCST.2011.2136435.
20. Hayes, A.D.; Caverly, R.J. Atmospheric-density-compensating model predictive control for targeted reentry of drag-modulated spacecraft. *J. Guid. Control Dyn.* **2025**, *48*, 2541–2556. https://doi.org/10.2514/1.G008665.
21. Lu, P.; Davami, C. Model predictive guidance: A fixed-point algorithm. *J. Guid. Control Dyn.* **2025**, *48*, 723–735. https://doi.org/10.2514/1.G008718.
22. Cheah, S.K.; Bhattacharjee, D.; Hemati, M.S.; Caverly, R.J. Control synthesis for hypersonic vehicle flight testing with input-output-sampled nonlinearities. *J. Guid. Control Dyn.* **2025**, *48*, 855–869. https://doi.org/10.2514/1.G008331.
23. Cao, R.; Lu, Y.P.; He, Z. System identification method based on interpretable machine learning for unknown aircraft dynamics. *Aerosp. Sci. Technol.* **2022**, *126*, 107593. https://doi.org/10.1016/j.ast.2022.107593.
24. Wang, Y.C.; Liu, Y.; Leibold, M.; Buss, M.; Lee, J. Hierarchical incremental MPC for redundant robots: A robust and singularity-free approach. *IEEE Trans. Robot.* **2024**, *40*, 2128–2148. https://doi.org/10.1109/TRO.2024.3370049.
25. Wang, Y.C.; Leibold, M.; Lee, J.; Ye, W.Y.; Xie, J.; Buss, M. Incremental model predictive control exploiting time-delay estimation for a robot manipulator. *IEEE Trans. Control Syst. Technol.* **2022**, *30*, 2285–2300. https://doi.org/10.1109/TCST.2022.3142629.
26. Ma, Z.W.; Wang, J.B.; Liang, Y.Q.; Zhou, D.; Chen, H.B. Real-time fault-tolerant guidance for launch vehicle ascending flight under thrust drop failure. *Acta Astronaut.* **2024**, *224*, 338–352. https://doi.org/10.1016/j.actaastro.2024.08.012.
27. Singer, R.A. Estimating optimal tracking filter performance for manned maneuvering targets. *IEEE Trans. Aerosp. Electron. Syst.* **1970**, *6*, 473–483. https://doi.org/10.1109/TAES.1970.310128.
28. Moose, R.L. An adaptive state estimation solution to the maneuvering target problem. *IEEE Trans. Autom. Control* **1975**, *20*, 359–362. https://doi.org/10.1109/TAC.1975.1100961.
29. Li, F.; Xiong, J.J.; Qu, Z.G.; Lan, X.H. A damped oscillation model for tracking near space hypersonic gliding targets. *IEEE Trans. Aerosp. Electron. Syst.* **2019**, *55*, 2871–2890. https://doi.org/10.1109/TAES.2019.2897517.
30. Zhang, S.; Guo, Y.; Lu, Z.X.; Wang, S.C.; Liu, Z.G. Cooperative detection based on the adaptive interacting multiple model-information filtering algorithm. *Aerosp. Sci. Technol.* **2019**, *93*, 105310. https://doi.org/10.1016/j.ast.2019.105310.
31. Wang, S.B.; Guo, Y.; Wang, S.C.; Liu, Z.G.; Zhang, S. Cooperative interception with fast multiple model adaptive estimation. *Def. Technol.* **2021**, *17*, 1905–1917. https://doi.org/10.1016/j.dt.2020.11.001.
32. Sun, Y.; Huang, D.C.; Shi, Z.Y.; Zhong, Y.S. Robust adaptive trajectory tracking control for fixed-wing unmanned aerial vehicles. *Aerospace* **2025**, *12*, 980. https://doi.org/10.3390/aerospace12110980.
33. Bianchi, D.; Di Gennaro, S.; Di Ferdinando, M.; Acosta Lùa, C. Robust control of UAV with disturbances and uncertainty estimation. *Machines* **2023**, *11*, 352. https://doi.org/10.3390/machines11030352.
34. Guo, Y.; Wang, S.C.; Yao, Y.; Yang, B.Q. Evader maneuver on consideration of energy consumption in flight vehicle interception scenarios. *Aerosp. Sci. Technol.* **2011**, *15*, 519–525. https://doi.org/10.1016/j.ast.2010.10.007.
35. Li, H.; Wang, Q.; Yu, J.L.; Piao, H.Y.; Lv, J.H.; Dong, X.W. Cooperative pinning game strategy against an attacking missile: Theory and experiment. *Sci. China Technol. Sci.* **2026**, *69*, 1100307. https://doi.org/10.1007/s11431-025-3120-6.

36. Reiner, J.; Balas, G.J.; Garrard, W.L. Flight control design using robust dynamic inversion and time-scale separation. *Automatica* **1996**, *32*, 1493–1504. https://doi.org/10.1016/S0005-1098(96)00101-X.
37. Wang, S.B.; Guo, Y.; Wang, Y.C.; Wang, S.C.; Li, C. Event-triggered incremental adaptive dynamic programming based model-free robust control for zero-sum game guidance. *IEEE Trans. Aerosp. Electron. Syst.* **2025**, *61*, 15438–15458. https://doi.org/10.1109/TAES.2025.3588825.
38. Lu, P.; van Kampen, E.; de Visser, C.; Chu, Q.P. Aircraft fault-tolerant trajectory control using incremental nonlinear dynamic inversion. *Control Eng. Pract.* **2016**, *57*, 126–141. https://doi.org/10.1016/j.conengprac.2016.09.010.
39. Simplicio, P.; Pavel, M.D.; van Kampen, E.; Chu, Q.P. An acceleration measurements-based approach for helicopter nonlinear flight control using incremental nonlinear dynamic inversion. *Control Eng. Pract.* **2013**, *21*, 1065–1077. https://doi.org/10.1016/j.conengprac.2013.03.009.
40. Wang, X.R.; van Kampen, E.; Chu, Q.P.; Lu, P. Stability analysis for incremental nonlinear dynamic inversion control. *J. Guid. Control Dyn.* **2019**, *42*, 1116–1129. https://doi.org/10.2514/1.G003791.
41. Zhang, Z.L.; Zhang, K.; Han, Z.G. Incremental nonlinear dynamic inverse-adaptive sliding mode three-dimensional angle constrained guidance law design. *IEEE Trans. Aerosp. Electron. Syst.* **2024**, *60*, 186–201. https://doi.org/10.1109/TAES.2023.3315718.

Disclaimer/Publisher's Note: The statements, opinions and data contained in all publications are solely those of the individual author(s) and contributor(s) and not of MDPI and/or the editor(s). MDPI and/or the editor(s) disclaim responsibility for any injury to people or property resulting from any ideas, methods, instructions or products referred to in the content.